3

Mechanisms for Grinding of Ceramics

S. Malkin and T.W. Hwang

CONTENTS

3.1 Introduction

Despite the development of advanced ceramic materials possessing enhanced properties, the widespread use of these materials for structural applications has been limited mainly because of the high cost of machining by grinding. In the manufacture of ceramic components, grinding can comprise up to 80% of the total cost [1]. Efficient grinding requires selecting

operating parameters to maximize the removal rate while controlling surface integrity [2,3]. Lowering grinding costs by using faster removal rates is constrained mainly by surface damage to the ceramic workpiece, which causes strength degradation. Any attempts to optimize the grinding parameters should take into account the prevailing grinding mechanisms and their influence on the resulting surface damage and mechanical properties.

The present chapter is concerned with what happens during grinding as abrasive grits interact with the ceramic workpiece. Most past research on grinding mechanisms for ceramics has followed either the ''indentation fracture mechanics'' approach or the ''machining'' approach [2]. The indentation fracture mechanics approach models abrasive–workpiece interactions with the idealized deformation and crack systems produced by an indentor. The machining approach typically involves measurement of forces for single-point and multipoint cutting coupled with microscopic observations of surface morphology and grinding debris. Both of these approaches provide important insights into the nature of the grinding process for ceramics.

3.2 Indentation Fracture Mechanics Approach

The indentation fracture mechanics approach likens abrasive–workpiece interactions for grinding of ceramics to small-scale indentation events. The deformation and fracture patterns observed for normal contact with a Vickers pyramidal indentor under an applied load P are illustrated in Figure 3.1. A zone of plastic deformation is found directly under the indentor. Two principal crack systems emanate from the plastic zone: median/radial and lateral cracks. Median/radial cracks are usually associated with strength degradation and lateral cracks with material removal.

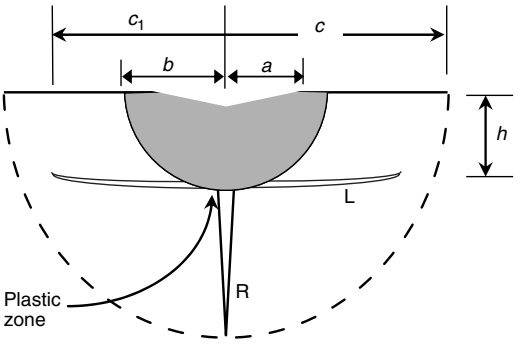

FIGURE 3.1
Plastic zone, median/radial cracks (R), and lateral cracks (L) for Vickers indentation. (From Lawn, B.R. and Swain, M.V., *J. Mater. Sci.*, 10, 113, 1975. With permission.)

Though originally developed for static normal loading, this approach has also been extended to include the effect of a tangential load (moving indentor).

3.2.1 Median/Radial Cracks: Static Indentor

Now let us consider how median/radial cracks can affect the strength degradation due to grinding. For this purpose, the normal applied load P on the indentor (abrasive grit) is considered to cause a median/radial crack of dimension c, as shown in Figure 3.1, which in turn leads to a reduction in the fracture strength. Larger cracks due to more severe grinding conditions and bigger forces should cause a greater reduction in the fracture strength after grinding.

Investigations of median/radial cracks using fracture mechanics started in the 1970s [4–11]. In one of the first studies, the median crack size was predicted using the Boussinesq solution for the elastic stress field due to point loading normal to the surface [4]. The stress intensity factor obtained by integrating the stress field around a median crack was used to predict the relationship between the applied load P and crack size c. Because elasticity predicts infinite stress at the contact point, the observed size of the deformation zone was taken as a lower limit on the integration. A proportional relationship was predicted between the load and crack length ($P \propto c$), which is consistent with experimental results for soda-lime glass [4]. However, in subsequent work [7], median crack extension was observed to occur not only during loading but also during unloading. This was attributed to nonuniform plastic deformation beneath the indentor, which causes residual stresses. Lateral cracking also occurred during unloading.

Many researchers have investigated the influence of plastic deformation and residual stresses on median/radial and lateral cracks [10–17]. An early study focused on resolving median crack propagation into two parts, an elastic component and an irreversible (residual) component [10,11]. The results suggest that the elastic component initiates the median crack and causes it to extend downward during loading, whereas the residual component provides continued crack extension, as the indentor is withdrawn. By modeling the indentation under the indentor as an expanding plastic zone surrounded by an elastic matrix, the stable crack size c (Figure 3.1) for a sharp pyramidal indentor after loading with force P and then unloading was obtained as [12]:

$$P/c^{3/2} = K_c \Big/ \left\{ \xi (\cot \psi)^{2/3} (E/H)^{1/2} \right\}, \tag{3.1}$$

where H is the hardness, E the elastic modulus, K_c the fracture toughness, 2ψ the included angle between opposite indentor edges, and ξ a constant. The relationship between load and crack size in Equation 3.1, $P \propto c^{3/2}$, fits the

experimental results quite well for many materials [12]. This relationship would apply only above a minimum threshold load P^* below which median cracks should not be initiated [9]:

$$P^* = 54.5(\alpha/\eta^2\gamma^4)(K_c^4/H^3), \tag{3.2}$$

where α, η, and γ are constants ($\alpha = 2/\pi$ for a Vickers indentor, $\eta \approx 1$, and $\gamma \approx 0.2$).

Although originally developed for a pyramidal indentor, a similar fracture mechanics analysis has also been developed for other indentor shapes. Assuming that the residual stress component is the main source of crack extension, the stress intensity factor for a penny-like crack was obtained as [17]:

$$K_r = \chi E(\delta V/V)^{1/3}(\delta V)^{2/3}/c^{3/2}, \tag{3.3}$$

where χ is a constant, V the plastic zone volume, and δV the indentation volume. To predict the relationship between load and crack size, it is necessary to relate δV and $\delta V/V$ to the applied load for different indentor shapes. The problem becomes greatly simplified by assuming the hardness to be independent of indentor shape, which is consistent with measurements for several brittle materials [13,18,19]. The hardness (indentation pressure) can be written as

$$H = P/\alpha_0 a^2, \tag{3.4}$$

where α_0 is a geometrical constant and a is a characteristic dimension of the indentation. The ratio $\delta V/V$ was also found to be independent of indentor shape and to follow a relationship of the form

$$\delta V/V \propto (H/E)^{3/2}. \tag{3.5}$$

For stable crack growth, combining Equation 3.3 and Equation 3.5 and equating K_r to K_c leads to

$$K_c = \chi(EH)^{1/2}(\delta V)^{2/3}/c^{3/2}. \tag{3.6}$$

For a pyramidal indentor, the indentation volume is

$$\delta V = (2/3)\, a^3 \cot\psi, \tag{3.7}$$

where a is half the diagonal length (Figure 3.1). Combining Equation 3.4, Equation 3.6, and Equation 3.7 would give the same load/crack length relationship as Equation 3.1 with $\xi = \{(2/3)^{2/3}/\alpha_0\}\chi$. For a spherical indentor of radius R,

$$(\delta V)^{2/3} = (\pi/4)^{2/3}R^2(a/R)^{8/3}, \tag{3.8}$$

where a is now the indentation radius. In this case, the load/crack length relationship becomes

$$P^{4/3}/c^{3/2} = (4\pi/R)^{2/3}\chi^{-1}(K_c E^{-1/2} H^{5/6}). \tag{3.9}$$

Therefore, the load/crack length relations in Equation 3.1 and Equation 3.9 predict $P \propto c^{3/2}$ for a pyramidal indentor and $P \propto c^{9/8}$ for a spherical indentor. This agrees quite well with experimental results in Figure 3.2 for ZnS.

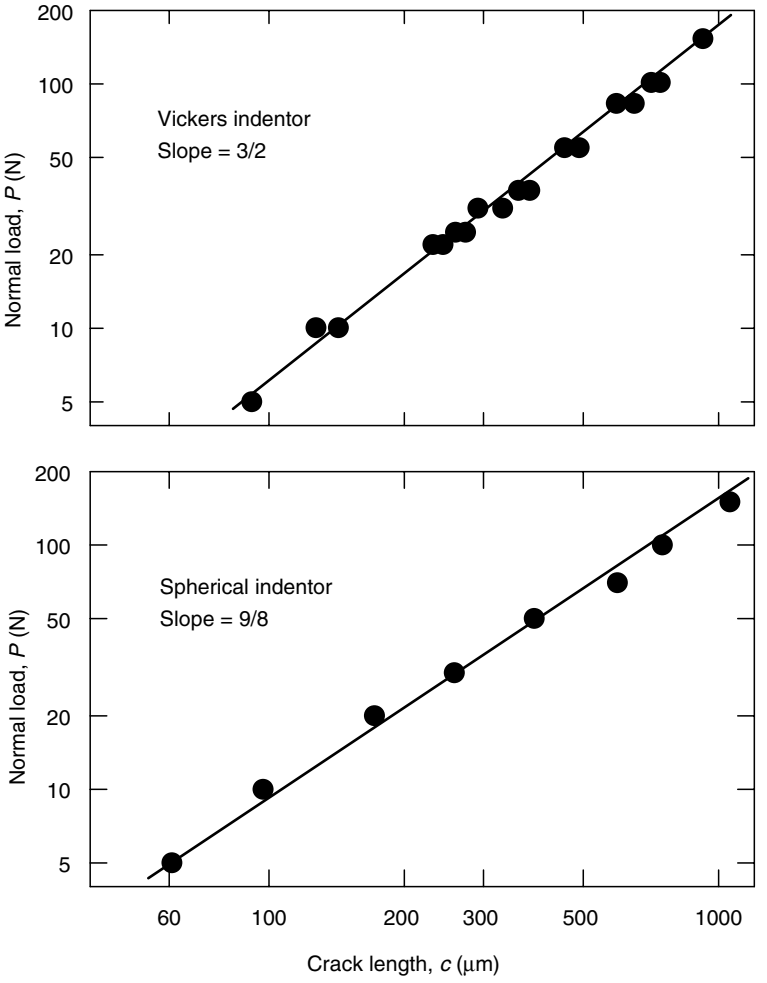

FIGURE 3.2
Load/crack length data for ZnS. (From Marshall, D.B., *J. Am. Ceram. Soc.*, 67, 57, 1984. With permission.)

As stated above, strength degradation is usually attributed to median/radial cracks and the influence of residual stresses on their extension [11,20–22]. The residual stress distribution for static indentation has been predicted [13] by superimposing the Boussinesq elastic stress field with the elastic/plastic solution for a spherical cavity under an internal pressure. The results indicate residual compressive stresses near the contact surface with a steep transition to tensile stresses reaching 0.1 to 0.15 H at the elastic/plastic boundary in the subsurface. Similar residual stress distributions have been reported for silicon nitride ceramics after grinding [23–25], but the peak residual tensile stresses are much smaller. For example, the peak residual tensile stress in Figure 3.3 is only about 0.007 H after grinding of hot-pressed silicon nitride (HPSN) [25]. Such small s tresses may not cause significant strength degradation. However, critical stress intensity factors evaluated from measurements of cracks produced by sharp indentors were about 30% less than those determined by double cantilever or double torsion tests [26,27], which suggests that the residual stresses due to indentation caused a 30% strength reduction.

According to fracture mechanics, the effect of crack size c on fracture strength σ_f can be written as

$$\sigma_f = K_{ic}/Yc^{1/2}, \tag{3.10}$$

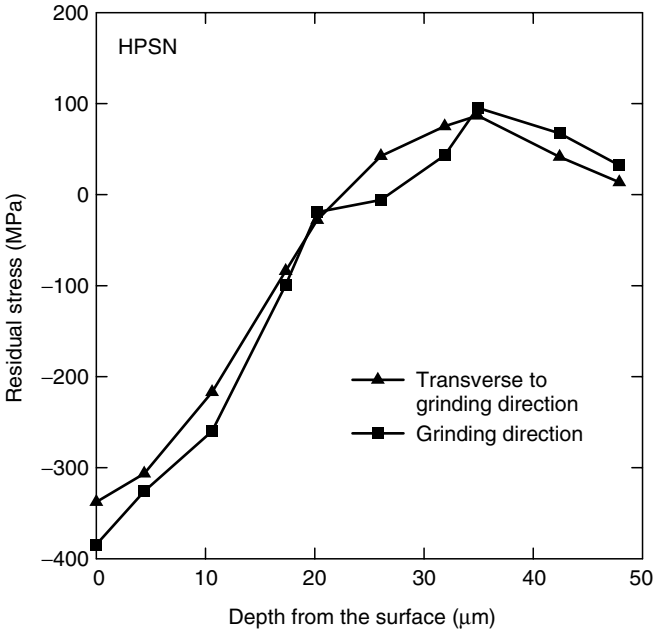

FIGURE 3.3
Residual stress versus depth for HPSN. (From Hakulinen, M., *J. Mater. Sci.*, 20, 1049, 1985. With permission.)

where K_{ic} is the fracture toughness and Y a constant that depends on crack geometry and orientation. When combined with the effect of load on crack size (Equation 3.1 and Equation 3.9), the influence of applied normal force on strength after indentation becomes

$$\sigma_f = A_p(H/E)^{1/6}(K_c^4/P)^{1/3} \tag{3.11}$$

for a pyramidal indentor ($A_p \equiv 1/\{Y(\xi)^{1/3}(\cot\psi)^{2/9}\}$) [20] and

$$\sigma_f = A_s(H^5/E^3)^{1/18}(K_c^3/P)^{4/9} \tag{3.12}$$

for a spherical indentor ($A_s \equiv (4\pi/R)^{2/9}/\{Y(\chi)^{1/3}\}$). Experimental results for a pyramidal indentor appear to correlate fairly well with Equation 3.11 for various ceramics and glasses [20].

By analogy with indentation, the formation of median cracks during grinding should result in a fracture strength relationship of the form [28]:

$$\sigma_f = \eta f_n^{-m}, \tag{3.13}$$

where f_n is the normal grinding force per grit analogous to the applied indentation load P. Experimental results for silicon nitride in Figure 3.4

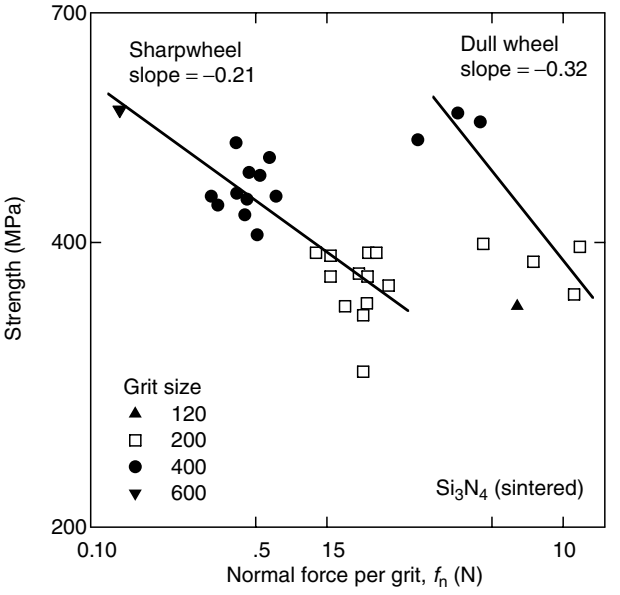

FIGURE 3.4
Flexural strength versus normal force per grit. (From Ota, M. and Miyahara, K., *4th Int. Grinding Conf.*, SME Technical Paper MR90–537, 1990. With permission.)

follow Equation 3.13 quite well with exponents $m = 0.21$ for a sharp wheel and $m = 0.32$ for a dull wheel, as compared with expected values of $m = 1/3$ for a pyramidal (sharp) indentor (Equation 3.11) and $m = 4/9$ for a spherical (dull) indentor (Equation 3.12). It should be noted that the forces per grit in Figure 3.4 are average values obtained by dividing the normal grinding force by the estimated number of active grits. Strength degradation should be dictated by the largest force per grit, which could be much bigger than the average. According to Equation 3.2, the threshold load for median crack formation with a pyramidal indentor for this material is approximately 3 N, which is probably smaller than the largest force per grit for most conditions in Figure 3.4.

3.2.2 Median/Radial Cracks: Moving Indentor

An active abrasive grit is subject not only to a normal load as in static indentation, but also to a tangential load in the direction of motion [29–32]. Analogous to the Boussinesq solution, the elastic stress field due to both a normal force component P and tangential component P' acting at a point on the surface has been modeled using the Michell solution [29]:

$$\sigma_{ij} = \left(\frac{P}{\pi r^2}\right)\left[f_{ij}(\theta,\phi)\right]_{\lambda,\mu} + \left(\frac{P'}{\pi r^2}\right)\left[g_{ij}(\theta,\phi)\right]_{\lambda,\mu}, \tag{3.14}$$

where λ and μ are Lame's constants and r, θ, and ϕ are polar coordinates. The tangential force tends to intensify the tensile stresses normal to the direction of motion ahead of the contact point. This would favor median crack propagation in the plane of motion [29], which could explain why test bars often exhibit more strength degradation when ground transversely than longitudinally. For example, results in Figure 3.5 [33] show strength degradation for transversely ground test bars above a critical uncut chip thickness (grit depth of cut) of about 0.16 μm, but not for longitudinally ground test bars. Similar strength anisotropy has also been reported for many other materials [34–42].

As with static indentation, the moving indentor also causes localized plastic deformation. Unlike static indentation, however, the normal contact pressure depends on the contact configuration and indentor geometry [30]. The median crack length has been predicted using an approximate plane strain plasticity analysis, which estimates the transverse crack-opening force perpendicular to the plane of motion. Although the average normal pressure is sensitive to indentor geometry, the predicted ratio of the transverse to normal force is approximately 0.35 for various indentors. The resulting load/crack size relationship is of the form $P \propto c^{3/2}$ [30], which is consistent with experimental results for glass [31], but not for other materials. For HPSN, the results in Figure 3.6 show approximately $P \propto c$ at

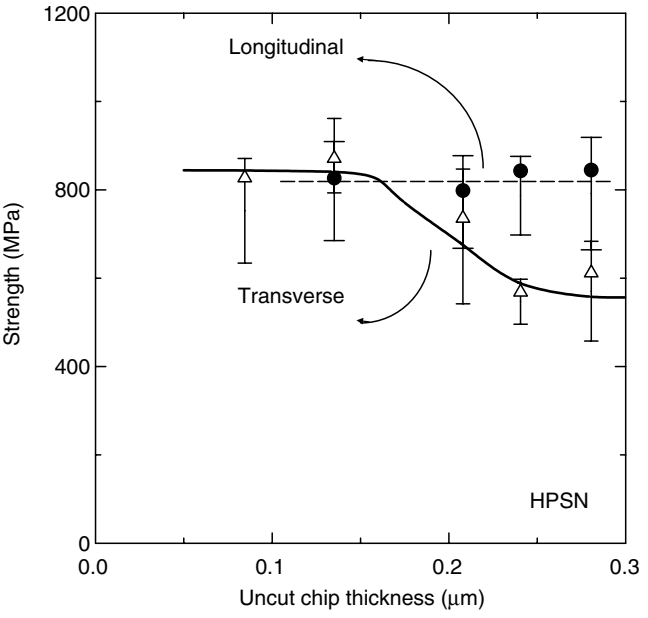

FIGURE 3.5
Transverse rupture strength versus uncut chip thickness for longitudinal and transverse grinding. (From Mayer, J.E., Jr. and Fang, G.P., *NIST SP* 847, 205, 1993. With permission.)

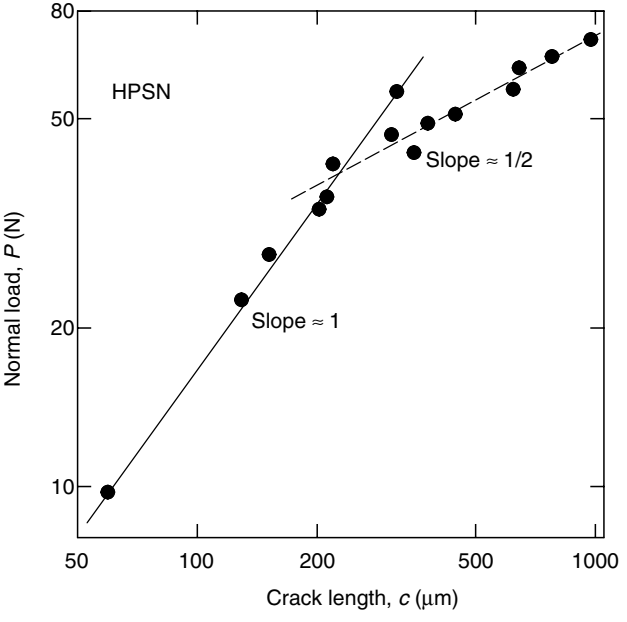

FIGURE 3.6
Normal load versus crack length. (From Kirchner, H.P., *J. Am. Ceram. Soc.*, 67, 127, 1984. With permission.)

low normal loads and $P \propto c^{1/2}$ at high loads [32]. The proportional relationship at low loads is consistent with the elastic solution for static indentation [4], so the influence of residual stress may be insignificant in this regime. However, at high loads, the residual stresses for a moving indentor could become the dominant factor. Analogous to static indentation with a spherical tool [17], the crack opening force determined from the residual stress field was related to the stress intensity factor. This elastic–plastic analysis for the moving indentor yields a load/crack length relationship $P \propto c^{1/2}$ [32]. Data in Figure 3.7 for both single-point and multipoint grinding suggest $P \propto c^{6/5}$ [31]. However, crack depths for multipoint grinding are only about half as big as for single-point grinding at the same normal loads. The indentor used in the scratching test is probably sharper than a typical abrasive grit, which might account for this difference. Another possible factor is the interactions between cracks from adjacent scratches in multipoint grinding, which could reduce the stress intensity factor [43,44].

Strength degradation resulting from single-point and multipoint grinding is associated with failures, which initiate from extended fracture origins induced by these events [31]. For an edge-notch crack, the predicted fracture strength would be given by Equation 3.10 with $Y = 1.99$. Experimental measurements of crack size and fracture strength for both single-point and multipoint grinding tests follow this behavior [31]. Analogous to the case of

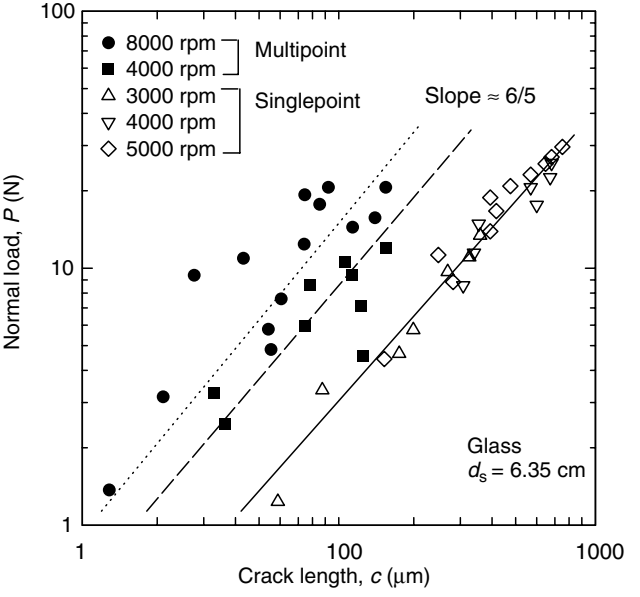

FIGURE 3.7
Normal load versus crack length. (From Kirchner, H.P., *J. Am. Ceram. Soc.*, 67, 347, With permission.)

static indentation, the fracture strength can be related in turn to the normal load if the load/crack size relationship is given. The load/crack size relationships for a moving indentor (scratching) and multipoint grinding are again of the form $P \propto c^{n}$ where $1/2 < n < 3/2$, which combined with Equation 3.13 yields a relation between fracture strength and normal load $\sigma_f \propto P^{-m}$ where $1/3 < m < 1$.

3.2.3 Lateral Cracking and Crushing

Whereas median/radial cracks are associated with strength degradation, lateral cracks may lead to material removal. Lateral cracks (Figure 3.1) initiate during unloading near the bottom of the plastic zone, and then propagate laterally on a plane nearly parallel to the specimen surface [6–8, 15]. Deflection of the crack toward the free surface can cause material removal by fracture (chipping). The effect of the applied load P on the lateral crack length c_ℓ has been estimated using simple plate theory [15]. If h is the distance from the free surface to the crack plane, the crack size for $c_\ell \gg h$ becomes [15]:

$$c_\ell = c^{L}\left[1 - (P_o/P)^{1/4}\right]^{1/2}, \tag{3.15}$$

where

$$P_o \equiv (\zeta_o/A^2)(\cot\psi)^{-2/3}(K_c^4/H^3)(E/H), \tag{3.16}$$

$$c^{L} \equiv \left\{\zeta_L \cot\psi^{5/6}\ A^{-1/2}(K_c H)^{-1}E^{3/4}\right\}^{1/2} P^{5/8}, \tag{3.17}$$

and ζ_o, ζ_L, and A are constants. At large contact loads ($P \gg P_o$), Equation 3.15 reduces to $P \propto c_\ell^{8/5}$, which is similar to the form for median/radial cracks.

An expression for the minimum threshold load for lateral cracking, P_ℓ^*, has been derived as [14,45]:

$$P_\ell^* = \zeta(K_c^4/H^3)f(E/H), \tag{3.18}$$

where ζ is a dimensionless constant and $f(E/H)$ is a weak function such that $\zeta f(E/H) \approx 2\times10^5$. Values for P_ℓ^* can be compared with average normal loads per grit to predict whether a lateral fracture mechanism or ductile removal mechanism might prevail [45]. For example, the normal force per grit for grinding of sintered silicon nitride (Figure 3.4) is less than the estimated critical threshold load of about 30 N, which would suggest ductile flow rather than lateral cracking. However, the predicted threshold load for median cracks (3 N for silicon nitride [9]) is much less than for lateral cracks,

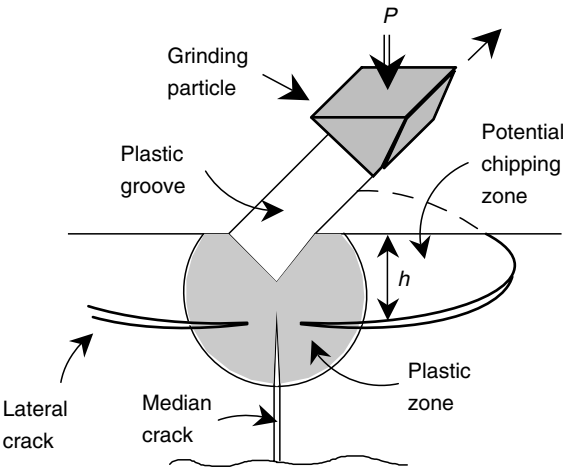

FIGURE 3.8
Plastic zone, median/radial, and lateral cracks for moving indentor. (From Evans, A.G. and Marshall, D.B., in *Fundamentals of Friction and Wear of Materials*, Rigney, D.A., Ed., ASME, 439, 1981. With permission.)

which would suggest that ductile grinding may produce median cracks and strength degradation.

The size of the lateral crack can be used to estimate abrasion (grinding) rates [45]. Assuming that the volume removed by a grit under a normal load P in Figure 3.8 is proportional to the lateral crack size and length of travel ℓ, the total volumetric removal V_ℓ is

$$V_\ell = \alpha_L (P^{9/8}/K_c^{1/2}H^{5/8})(E/H)^{4/5}\ell, \tag{3.19}$$

where α_L is a constant. This expression correlates fairly well with some limited data for grinding of ceramics only at extremely small removal rates [45,46]. Evidence of material removal by lateral cracking is often observed on scratched grooves.

In addition to lateral cracking, material removal by fracture has also been related to crushing [32,47–49]. Crushing ahead of and beneath the contact has been attributed to mixed mode fracture resulting from the distribution of in-plane hoop stresses and shear stresses [29]. The crushed zone boundary beneath a moving indentor has been estimated by assuming that crushing occurs by fractures originating at distributed preexisting flaws where the elastic strain energy density exceeds a critical value [48]. A somewhat more comprehensive model was subsequently developed which attributes crushing to sequential crack branching under a moving indentor [49]. This latter model successfully predicted crushing depths for single-point grinding of glass, but over predicted crushing depths for HPSN [49].

These differences may be related to the assumption of a purely elastic stress field. Localized plastic deformation, which should be more significant for the silicon nitride, would reduce the stress intensity and crushing depth.

3.3 Machining Approach

The machining approach typically involves measurement of cutting forces and energy together with microscopic observations of grinding debris and surface morphology. Although microscopic observations provide important evidence about the prevailing grinding mechanisms, any plausible physical model of abrasive–workpiece interactions must be able to quantitatively account for the magnitude of the grinding energy and its dependence on the operating conditions.

3.3.1 Grinding Debris

Examination of grinding debris for various brittle materials [33,50–53] suggests material removal mainly by brittle fracture. For example, SEM micrographs of grinding debris collected for reaction bonded silicon nitride (RBSN) ground with a 400 grit diamond wheel are shown in Figure 3.9. The debris consists mostly of relatively large plate-like particles (Figure 3.9a) which appear to have fractured from the workpiece by lateral cracking, and much finer particles (Figure 3.9b) which may have been generated by crushing. The plate-like particles typically have grinding striations on one side as seen in Figure 3.9a. The striations may have been generated either immediately before the particle fractured from the workpiece or during the preceding grinding pass.

Grinding debris generation has also been studied in-process using a camera equipped with a micro-flash [50]. Many fine particles were observed flying off both ahead of and just behind the grit, which suggests material dislodged by lateral cracking crushed into smaller particles. Crushing (pulverization) may also be responsible for much finer particles (powder) beneath the scratched groove [54,55]. Aside from brittle fracture particles, continuous flow-type chips are also occasionally observed at high grinding speeds and shallow depths of cut [50,56], which would indicate ductile flow.

3.3.2 Microscopy of Scratches and Ground Surfaces

A detailed picture of the prevailing mechanisms has been developed from microscopic observations of scratches produced by single-point diamond

(a)

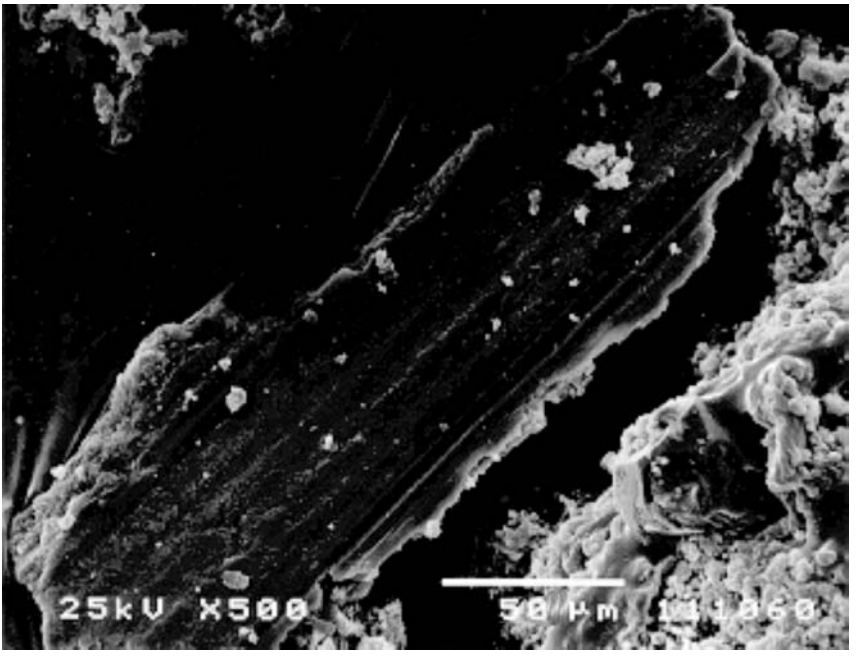

(b)

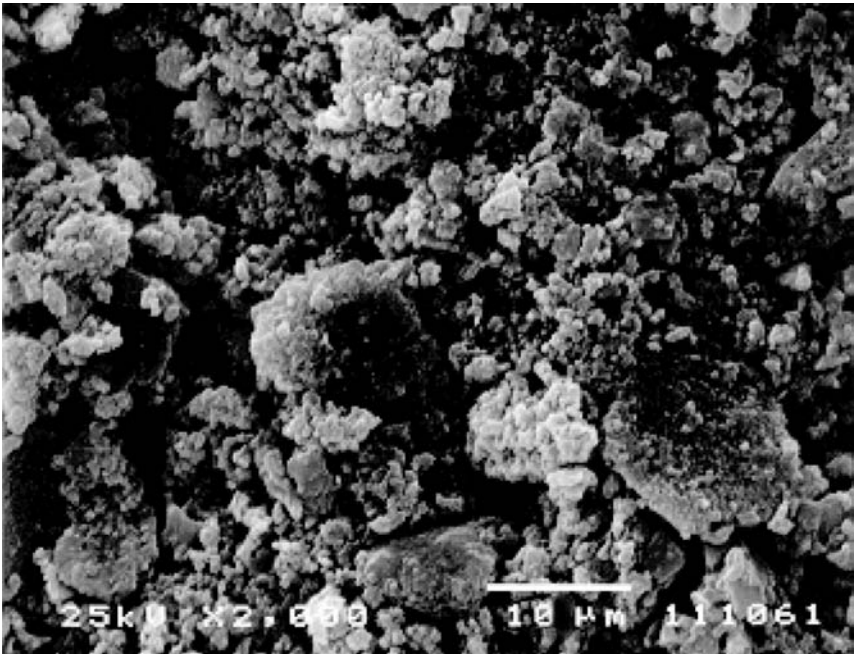

FIGURE 3.9
Grinding debris, RBSN (Coors/Eaton), 400 grit wheel (Norton) [65]: (a) $a = 38$ µm, $v_w = 200$ mm/sec, $v_s = 10$ m/sec; (b) $a = 22$ µm, $v_w = 100$ mm/sec, $v_s = 32$ m/sec.

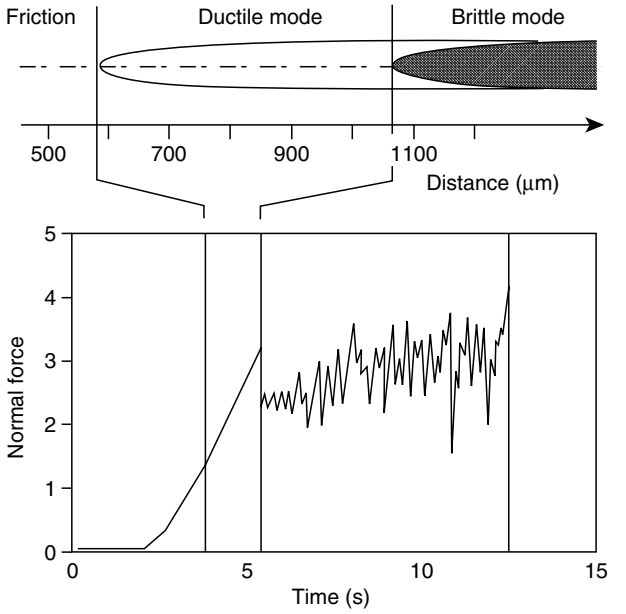

FIGURE 3.10
Cutting regimes for silicon. (From Brinksmeier, E., Preub, W., and Riemer, O., *Proc. 8th Int. Prec. Eng. Sem.*, 335, 1995. With permission.)

tools [31,32,47,54,57–63]. Scratching experiments performed with fixed depths of cut on silicon nitride [32] and alumina [58] show evidence of ductile flow, lateral cracking and chipping along the groove, and crushing beneath and ahead of tool with an increased depth. However, in most actual grinding processes, the depth of cut progressively increases as the abrasive grit passes through the grinding zone. This behavior has been simulated with single-point cutting by inclining the workpiece in the cutting direction. For inclined single-point cutting of silicon and germanium [61], initial ductile flow progressively changed to brittle fracture after a critical depth of cut was reached (Figure 3.10). The normal force increased linearly with distance (depth of cut) in the ductile regime, and then fluctuated about a lower value as brittle fracture occurred.

Grinding involves a multitude of scratches and interactions between adjacent scratches. The effect of interactions between adjacent scratches on stock removal has been investigated for hot-pressed alumina by making a series of parallel scratches with separation distances from 0 to 250 μm [64]. The results in Figure 3.11 show a strong dependence on the separation distance, as well as the load. Either when the separation is so large that the scratches do not interact or small enough to overlap, material removal is

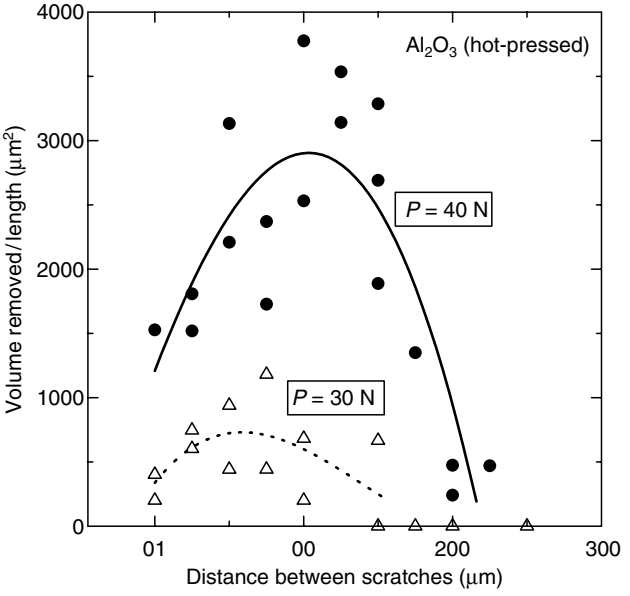

FIGURE 3.11
Material removed per unit length versus distance between scratches. (From Xu, H.H.K., Jahanmir, S., and Wang, Y., *J. Am. Ceram. Soc.*, 78, 881, 1995. With permission.)

relatively small. At intermediate distances, the removal becomes much bigger.

SEM micrographs in Figure 3.12 show HPSN surfaces ground with a 180 grit diamond wheel before etching (Figure 3.12a) and after etching (Figure 3.12b) with hydrofluoric acid [65]. Although some fractured areas can be seen, the as-ground surface exhibits mainly ductile flow associated with plowing along the grinding direction. However, after etching, many of the finer striations disappear whereas grooves generated by abrasive grits can still be seen. Etching of the ground silicon nitride surfaces with hydrofluoric acid appears to have removed a smeared glassy layer. The formation of glassy material on silicon nitride surfaces during sliding can be attributed to the oxidation reaction [66]:

$$Si_3N_4 + 3O_2 \rightarrow 3SiO_2 + 2N_2. \tag{3.20}$$

Silicon oxide glassy layers have also been recently identified on ground silicon surfaces [67] using energy dispersive spectroscopy.

3.3.3 Grinding Energy and Mechanisms

A fundamental parameter derived from the grinding forces and machining conditions is the specific grinding energy, which is defined as the energy

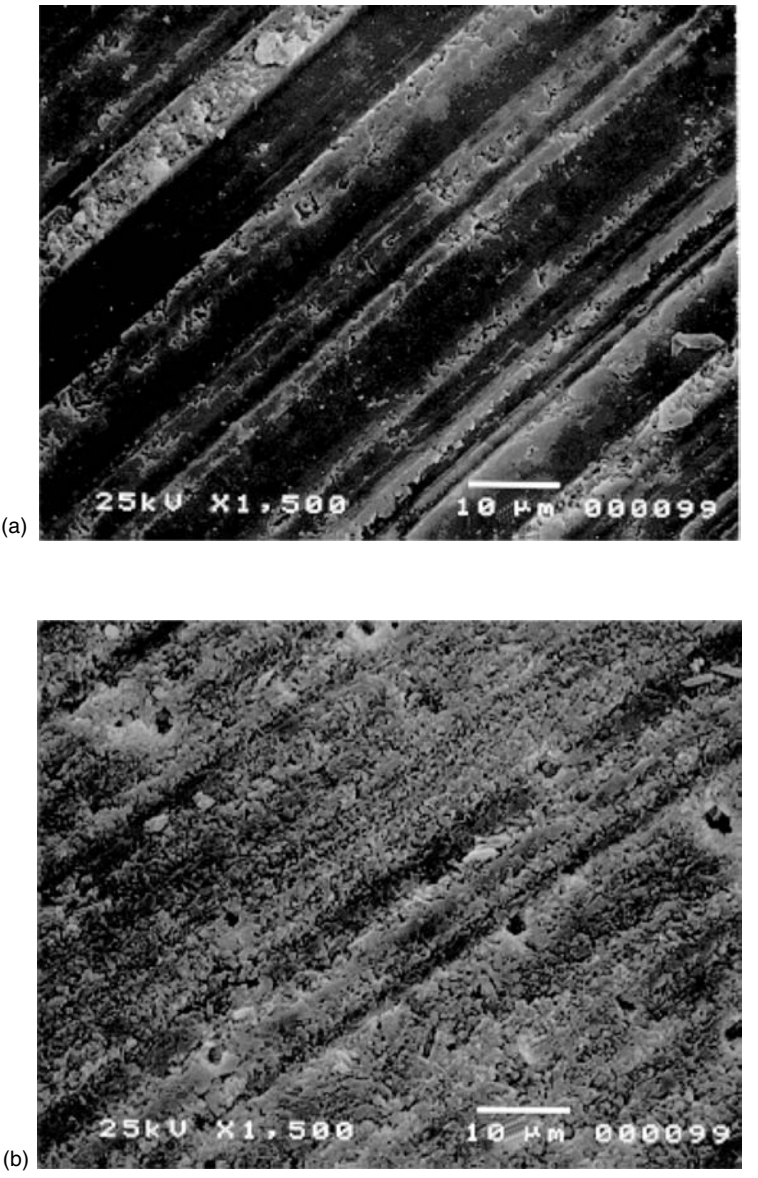

FIGURE 3.12
Ground surfaces, HPSN (Kyocera SN220), 180 grit wheel Norton ($a = 38$ µm, $v_w = 100$ mm/sec, $v_s = 32$ m/sec) (a) as ground; (b) after etching. (From Hwang, T.W. and Malkin S., *ASME J. Manuf. Sci. Eng.*, 121, 623. With permission.)

per unit volume of material removal. The specific energy is obtained from the relationship [68]:

$$u = \frac{F_t v_s}{Q_w} = \frac{P_m}{Q_w}, \tag{3.21}$$

where F_t is the tangential grinding force, v_s the wheel velocity, P_m the net grinding power, and Q_w is the volumetric removal rate. For metallic workpiece materials, the total specific grinding energy can be modeled as the sum of chip formation, plowing, and sliding components [68]. For ceramics and other brittle materials, the relationship between the grinding mechanisms and specific energy is complicated by the occurrence of both brittle fracture and ductile flow.

3.3.3.1 Specific Grinding Energy

Force and grinding energy data have been obtained for various ceramics over a wide range of conditions [69–75]. For straight surface grinding of HPSN, specific energies have been reported ranging from about 10 J/mm^3 at very high removal rates to about 800 J/mm^3 at very low removal rates [65,69–71]. A simple explanation for this type of behavior is that a decrease in removal rate results in a smaller undeformed (uncut) chip size, causing more flow and less brittle fracture. Results for specific grinding energy versus average uncut chip cross-sectional area in Figure 3.13 for aluminum oxide and silicon nitride show two distinct regimes [72]. Below an average uncut chip area of about 0.05 μm^2, which would correspond to a maximum undeformed chip thickness of about 0.35 μm (see Equation 3.23), the specific energy increases steeply with smaller chip size. Above the transition, the specific energy decreases more slowly as the chip size increases. The undeformed chip thickness at the transition may correspond to the critical threshold depth of cut, d_c corresponding to the critical load (Equation 3.18) below which fracture should not occur [76]:

$$d_c = \beta(E/H)(K_c/H)^2, \tag{3.22}$$

where β is a constant. Although the maximum undeformed chip thickness of 0.35 μm at the transition is somewhat bigger than the value computed from Equation 3.22 with $\beta = 0.15$, these results suggest material removal mainly by ductile flow below the transition and brittle fracture above the transition.

The magnitude of the specific grinding energy and its dependence on the operating parameters is a direct consequence of the prevailing grinding mechanisms. One parameter, which has been used to analyze specific grinding energy data, is the maximum undeformed (uncut) chip thickness taken by an individual cutting point (grit depth of cut) which can be written as [68]:

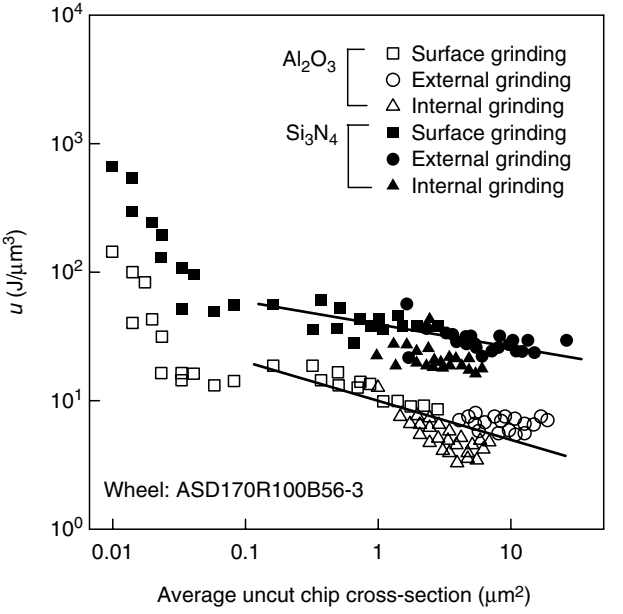

FIGURE 3.13
Specific energy versus average uncut chip cross-sectional area. (From Chen, C., Jung, Y., and Inasaki, I., in *Grinding Fundamentals and Applications*, Malkin, S. and Kovach, J.A., Eds., 39, 201, 1989. With permission.)

$$h_m = \left[\frac{3}{C\tan\theta}\left(\frac{v_w}{v_s}\right)\left(\frac{a}{d_s}\right)^{1/2}\right]^{1/2}, \tag{3.23}$$

where C is the active cutting point density, v_w the workpiece velocity, a the wheel depth of cut, d_s the wheel diameter, and θ is the semiincluded angle for the undeformed chip cross-section assumed to be triangular as illustrated in Figure 3.14. Experimental results for the specific energy obtained from various ceramics and a glass as listed in Table 3.1 are plotted versus h_m in Figure 3.15 for a 400 grit resin-bonded diamond wheel and in Figure 3.16 for a 180 grit wheel [77]. Results for the various workpiece materials with both wheels showed the same type of inverse behavior, a decrease in specific energy with h_m at a diminishing rate toward a minimum value. Each set of results in Figure 3.15 and Figure 3.16 was statistically fitted by least squares to an equation of the form:

$$u = \frac{A_s}{h_m} + B_s, \tag{3.24}$$

where A_s and B_s are constants. Values of A_s and B_s obtained by least square fitting are included in Table 3.1. The fitted curves shown in Figure 3.15 and

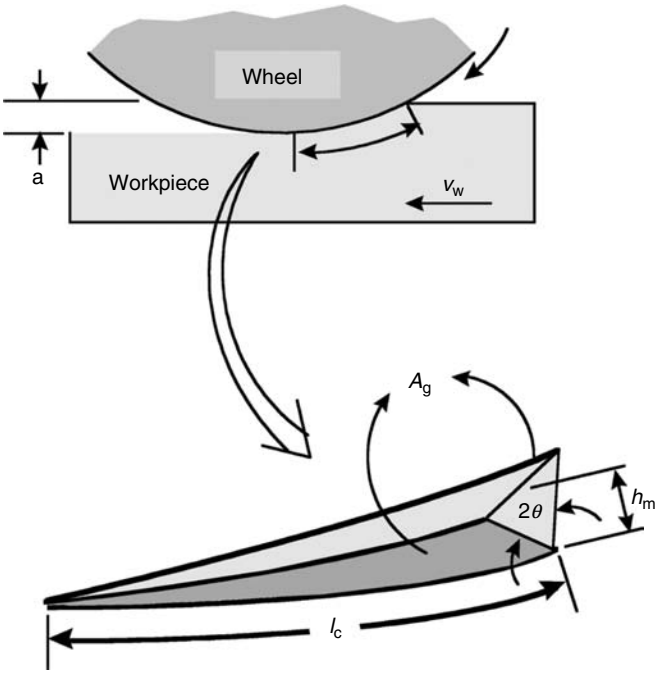

FIGURE 3.14
Illustration of undeformed chip geometry. (From Hwang, T.W. and Malkin, S., *ASME J. Manuf. Sci. Eng.*, 121, 623. With permission.)

Figure 3.16 represent the grinding behavior quite well except perhaps for the RBSN workpiece. The correlation coefficients for least square fitting were all in excess of 0.9 except for the RBSN. It can be seen in Table 3.1 that both A_s and B_s values for the 400 grit wheel are bigger than those for the 180 grit wheel on the same HPSN (Norton NC132), workpiece material. For the RBSN in Figure 3.15b, a better fit may be obtained using a stronger inverse relationship with h_m.

3.3.3.2 Brittle Fracture Energy

The relationship between the specific grinding energy and the undeformed chip thickness as described above should be related to the grinding mechanisms. It has been suggested that removal mechanisms at small values of h_m are dominated by high energy ductile flow (ductile regime) because the force acting on each grit is less than the critical load for lateral cracking to occur. The lower specific energy and bigger forces per grit at large values of h_m might indicate material removal by brittle fracture.

This explanation for the influence of h_m on the specific energy would imply that the minimum specific energy B_s should be comparable to the

TABLE 3.1

Experimental Grinding Conditions, Workpiece Properties, Fitted Values of A_s and B_s for Plots of Specific Energy Versus h_m, and Estimated Plowed Surface Energies Per Unit Area J_s and Correlation Coefficients r

Wheel	C (mm^{-2}) d_g (μm)	Grinding Parameters	Workpiece Material	E (GPa)	H (GPa)	K_c (MPa $m^{1/2}$)	$G_c/2$ (J/m^2)	A_s (10^3 J/m^2)	B_s (J/mm^3)	J_s (J/m^2)	r
DN400-	$C = 107$	$a = 5 \sim 38$ μm	S/RBSN	297	15.0	6.6	73.3	11.4	32.9	15,300 ± 1,520	0.83
N100B-1/4	$d_g = 38$	$v_w = 5 \sim 200$ mm/sec	RBSN*	165	10.0	3.6	39.3	35.3	0.0	4,700 ± 245	0.94
			HPSN[1]	325	19.6	5.0	38.5	15.4	28.7	18,000 ± 705	0.96
		$v_s = 10 \sim 40$	Al_2O_3	380	13.3	4.5	26.6	9.1	10.5	7,900 ± 255	0.97
DN180-	$C = 21$	$a = 5 \sim 76$ μm	HPSN[1]	325	19.6	5.0	58.9	9.1	16.7	14,200 ± 585	0.95
N100B-1/4	$d_g = 84$	$v_w = 5 \sim 200$ mm/sec	HPSN[2]	276	18.2	5.7	38.5	4.9	16.6	15,900 ± 365	0.98
			SiC[1]	410	27.4	3.5	14.9	6.4	7.4	10,000 ± 400	0.96
		$v_s = 10 \sim 40$ m/sec	SiC[2]	427	27.0	3.0	10.5	5.5	7.0	9,100 ± 590	0.91
			Glass**	70	5.5	0.75	4.0	2.0	1.0	1,800 ± 85	0.95

HPSN[1]—Norton NC132, HPSN[2]—Kyocera SN220, SiC[1]—Carborundum, Hexoloy SA, SiC[2]—Norton, Glass—Soda-lime Glass, S/RBSN—Coors/Eaton, RBSN—Coors/Eaton, Al_2O_3—Wesgo, Al995.

Source: *From Hwang, T.W., 1997, Grinding energy and mechanisms for ceramics, PhD Thesis, University of Massachusetts.

**From Lawn, B.R. and Evans, A.G., 1980, *J. Am. Ceram. Soc.*, Vol. 63, pp. 574–581.

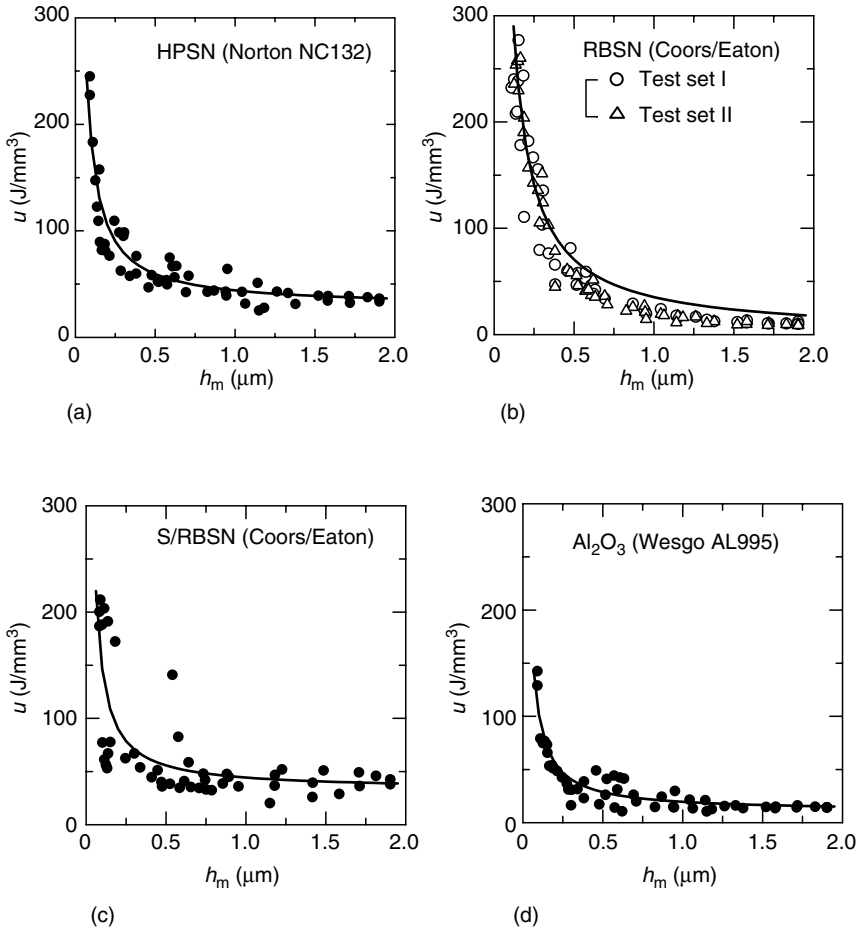

FIGURE 3.15
Specific grinding energy versus undeformed chip thickness (Norton 400 grit diamond wheel).

energy for material removal by brittle fracture. That portion of the grinding energy associated with brittle fracture can be estimated as the product of the surface area generated by fracture and the material's fracture energy per unit area [51]. For simplicity, the particles removed by grinding can be assumed small cubes of dimension b_f. In this case, the total surface area produced per unit volume of material removed, a_f, is equal to the total surface area of a cube divided by its volume:

$$a_f = \frac{6b_f^2}{b_f^3} = \frac{6}{b_f}. \tag{3.25}$$

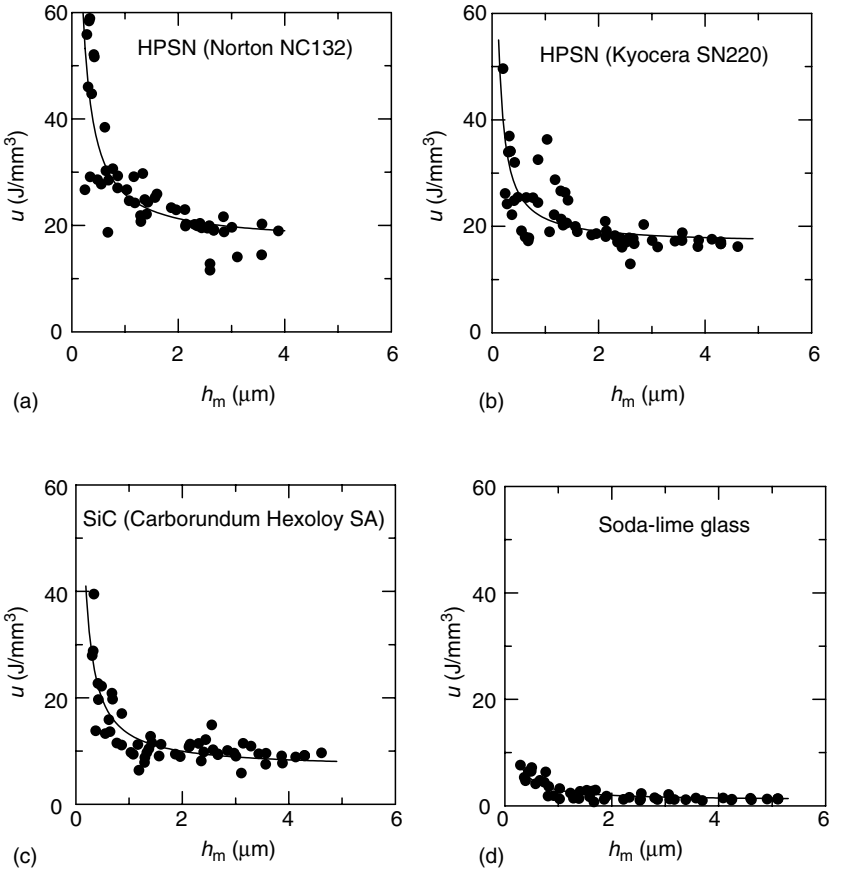

FIGURE 3.16
Specific grinding energy versus undeformed chip thickness (Norton 180 grit diamond wheel).

Approximating the fracture surface energy as half the critical energy release rate G_c ($G_c = {K_c}^2/E$) for crack formation (two surfaces), the specific energy due to fracture becomes

$$u_f = \left(\frac{G_c}{2}\right) a_f = \frac{3G_c}{b_f}. \tag{3.26}$$

The smallest particles removed by grinding are approximately 1 μm in size, although many are much larger. For HPSN, $G_c \approx 80\ \mathrm{J/m^2}$. Using these values for b_f and G_c leads to a specific fracture energy $u_f \approx 0.24\ \mathrm{J/mm^3}$, which is only a negligible portion of the extrapolated minimum grinding energy for

HPSN. This same argument would also apply to all the other workpiece materials as listed in Table 3.1 with the possible exception of RBSN. Therefore, most of the grinding energy must be expended by ductile flow, even though material removal is mainly by brittle fracture.

3.3.3.3 Plowed Surface Area Analysis

SEM observations reveal characteristic grooves and a heavily deformed layer on the ground surface. The generation of this deformed surface layer is apparently related to plowing by numerous abrasive points passing through the grinding zone, thereby leading to surfaces with multiple overlapping scratches and grooves. Therefore, it might also be worthwhile to analyze the grinding energy in terms of the plowed area generated on the workpiece by the active abrasive cutting points.

For the purpose of estimating the plowed surface area, again consider the plowing geometry for a single undeformed chip with a triangular cross-section of semiincluded angle θ as shown in Figure 3.14. Assuming that the active cutting points per unit area C are uniformly distributed on the wheel surface, the undeformed chip thickness h_m is given by Equation 3.23 [68]. For each undeformed chip as shown in Figure 3.14, the corresponding plowed surface area A_g generated at the sides of the groove is given by

$$A_g = \frac{h_m l_c}{\cos\theta}. \tag{3.27}$$

Multiplying by the number of cutting points per unit time per unit width of grinding leads to an expression for the overall rate of plowed surface area generated per unit width [65]:

$$S'_w = C v_s A_g. \tag{3.28}$$

Substituting for h_m from Equation 3.23 and noting that $l_c = (a d_s)^{1/2}$ results in

$$S'_w = \left(\frac{6C}{\sin 2\theta}\right)^{1/2} (v_w v_s)^{1/2} (a)^{3/4} (d_s)^{1/4}. \tag{3.29}$$

A plot of the measured power per unit width for HPSN (Norton NC132) ground with both a 400 grit wheel ($C = 107\ \text{mm}^{-2}$) and 180 grit wheel ($C = 21\ \text{mm}^{-2}$) versus the corresponding values of S'_w with $\theta = 60$ degrees is presented in Figure 3.17. A nearly proportional relationship is obtained between power per unit width and S'_w. Similar behavior was found with all the other wheel/workpiece combinations listed in Table 3.1. Each plot of the measured power per unit width versus the rate of plowed surface area generated per unit width was fitted to a linear relationship of the form:

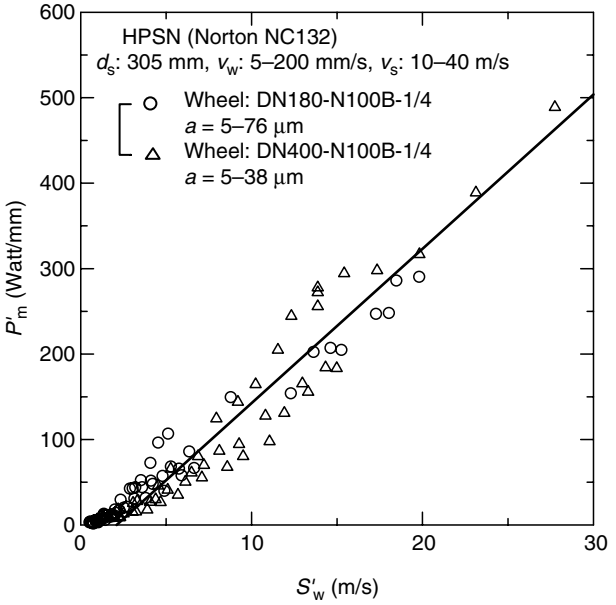

FIGURE 3.17
Power per unit width versus rate of plowed surface area generated per unit width.

$$P'_m = J_s S'_w + B_p, \tag{3.30}$$

where J_s and B_p are constants. Assuming that the total grinding energy is associated only with plowing and neglecting the influence of the intercept B_p, the slope J_s would correspond to the average energy per unit area of plowed surface generated. The slopes J_s obtained for various workpiece materials together with their standard errors and correlation coefficients r for least square fitting of the data are included in Table 3.1. The values of J_s are typically about two orders of magnitude bigger than the corresponding fracture surface energies ($G_c/2$ in Table 3.1), which is a further indication that most of the energy dissipation is associated with ductile flow.

3.3.3.4 Plowed Surface Energy and Workpiece Properties

According to the analysis presented above, J_s represents the surface energy per unit area generated by plowing. Estimated values for J_s in Table 3.1 are nearly constant for a given workpiece material regardless of the grinding conditions and grit size. Therefore J_s might be considered to be a ''characteristic'' material property which depends on the mechanical properties of the workpiece (E, H, and K_c) included in Table 3.1.

A number of attempts were made to correlate J_s with E, H, and K_c [65]. J_s generally tends to increase with H, and K_c, but no satisfactory correlation was found with any one of these three mechanical properties. Therefore, correl-

ations were attempted with combinations of material properties. From indentation fracture mechanics, the volumetric material removal per unit length of travel by scratching with a pyramidal tool has been theoretically related to the lateral crack size and the mechanical properties [8,45]. For a given volumetric removal per unit length of travel, this leads to a relationship between the normal load P and the mechanical properties, which can be written as [8]:

$$(P)^{5/4} \propto (K_c^{3/4} H^{1/2}) \tag{3.31}$$

or using a modified analysis [45]:

$$(P)^{9/8} \propto (K_c^{1/2} H^{5/8}). \tag{3.32}$$

Therefore J_s for a given volume removal per unit length might be related to the combined mechanical properties on the right hand side of Equation 3.31 and Equation 3.32, namely $K_c{}^{3/4}H^{1/2}$ and $K_c{}^{1/2}H^{5/8}$. A plot of J_s versus $K_c{}^{3/4}H^{1/2}$ presented in Figure 3.18 yields quite a good correlation, with J_s proportional to $(K_c{}^{3/2}H^{1/2})^2$. A proportional relationship between J_s and $(K_c{}^{1/2}H^{5/8})^{9/5}$ in Figure 3.19 shows somewhat more deviation, especially for silicon carbide ceramics.

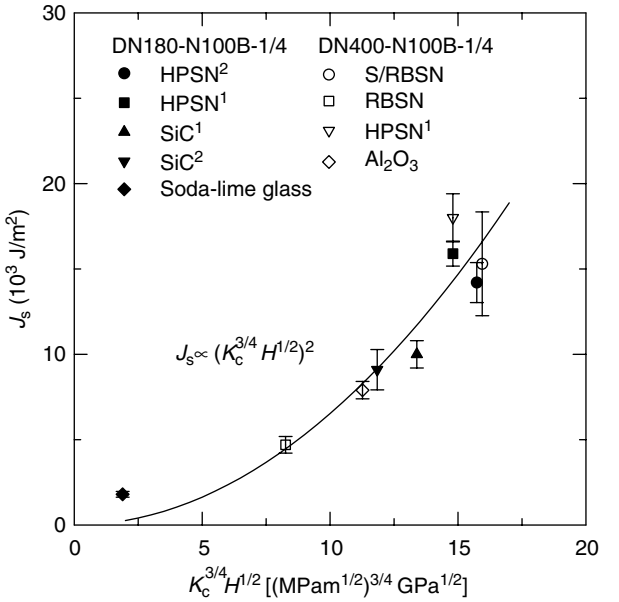

FIGURE 3.18
Plowed surface energy per unit area versus $K_c{}^{3/2}H^{1/2}$. (From Hwang, T.W. and Malkin, S., *ASME J. Manuf. Sci. Eng.*, 121, 623. With permision.)

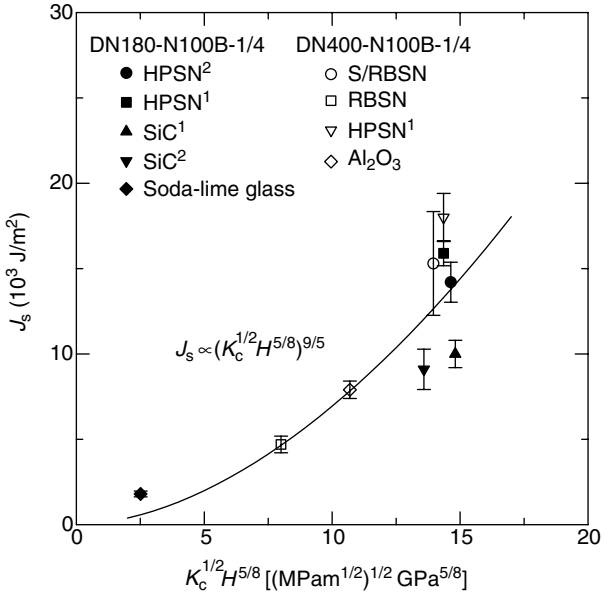

FIGURE 3.19
Plowed surface energy per unit area versus $K_c^{1/2}H^{5/8}$. (From Hwang, T.W. and Malkin, S., *ASME J. Manuf. Sci. Eng.*, 121, 623. With permission.)

The results in Figure 3.18 would indicate that $J_s \propto K_c^{3/2}H$. Therefore, the grinding power per unit width should be proportional to the product of $K_c^{3/2}H$ and the rate of plowed area generated per unit width. Indeed all the results in Figure 3.20 (540 data points as indicated in Table 3.1) of P_m' versus $K_c^{3/2}HS_w'$ tend to fall close to the same straight line. For all the materials ground over a wide range of conditions, the net grinding power per unit width can be approximated as:

$$P_m' = MK_c^{3/2}HS_w', \tag{3.33}$$

where $M \approx 6.4\times10^{-20}\ \mathrm{N^{-3/2}m^{13/4}}$.

3.4 Concluding Remarks

Most past research on grinding mechanisms for ceramics has followed either the ''indentation fracture mechanics'' approach or ''machining'' approach. The indentation fracture mechanics approach would seem to offer the possibility of describing both the material removal process and its influence on strength degradation in terms of the force or depth of cut at an

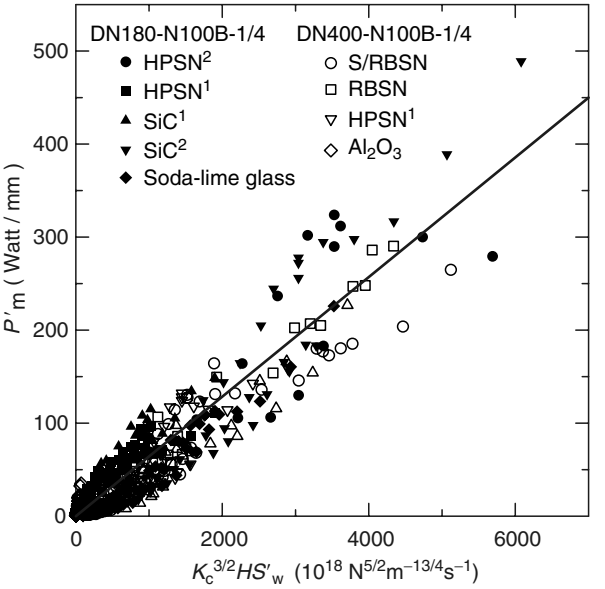

FIGURE 3.20
Grinding power per unit width versus $K_c^{3/2} HS'_w$. (From Hwang, T.W. and Malkin, S., *ASME J. Manuf. Sci. Eng.*, 121, 623. With permission.)

individual cutting point. Furthermore, it predicts the possibility of ductile regime grinding at extremely low removal rates where the force or depth of cut per grit is below a critical value. While providing some important insights into what may occur during abrasive–workpiece interactions, this approach has had limited quantitative application to realistic grinding operations. Its application is complicated by the grit geometry, interactions between grinding scratches, and elevated temperatures at the grinding zone.

From the machining approach, it has become evident that material removal for grinding of ceramics occurs mainly by brittle fracture, although most of the grinding energy is associated with ductile flow due to plowing. A new plowing model has been developed which quantitatively accounts for the grinding energy by relating the grinding power to the rate of plowed surface area generated. Over a wide range of grinding conditions, the power was found to be nearly proportional to the rate of plowed surface area generated, which suggests a nearly constant energy per unit area of plowed surface J_s. Values for J_s are much bigger than the corresponding fracture surface energies and are proportional to $K_c^{3/2}H$. Much additional research is needed to evaluate the general validity of this plowing model and its applicability to different types of grinding operations.

References

1. Kovach, J.A., Blau, P.J., Malkin, S., Srinivasan, S., Bandyopadhyay, B., and Ziegler, K., 1993, A feasibility investigation of high speed, low damage grinding process for advanced ceramics, *5th Int. Grinding Conf.*, Vol. I, SME.
2. Malkin, S. and Hwang, T.W., 1996, Grinding mechanisms for ceramics, *Ann. CIRP*, Vol. 45/2, pp. 569–580.
3. Verlemann, E., 1993, Technologies and strategies for the machining of ceramic components, *Ceramic Monographs*, No. 1.8.3.1, Varley Schmid GmbH.
4. Lawn, B.R. and Swain, M.V., 1975, Microfracture beneath point indentations in brittle solids, *J. Mater. Sci.*, Vol. 10, pp. 113–122.
5. Hockey, B.J., 1971, Plastic deformation of aluminum oxide by indentation and abrasion, *J. Am. Ceram. Soc.*, Vol. 54, pp. 223–231.
6. Lawn, B.R. and Wilshaw, T.R., 1975, Indentation fracture: principles and applications, *J. Mater. Sci.*, Vol. 10, pp. 1049–1081.
7. Lawn, B.R. and Fuller, E.R., 1975, Equilibrium penny like cracks in indentation fracture, *J. Mater. Sci.*, Vol. 10, pp. 2016–2024.
8. Evans, A.G. and Wilshaw, T.R., 1976, Quasi-static solid particle damage in brittle materials: I, *Acta Metall.*, Vol. 24, pp. 939–956.
9. Lawn, B.R. and Evans, A.G., 1977, A model of crack initiation in elastic/plastic indentation fields, *J. Mater. Sci.*, Vol. 12, pp. 2195–2199.
10. Marshall, D.B. and Lawn, B.R., 1979, Residual stress effects in sharp contact cracking: part 1: indentation fracture mechanics, *J. Mater. Sci.*, Vol. 14, pp. 2001–2012.
11. Marshall, D.B., Lawn, B.R., and Chantikul, P., 1979, Residual stress effects in sharp contact cracking: part 2: strength degradation, *J. Mater. Sci.*, Vol. 14, pp. 2225–2235.
12. Lawn, B.R. and Evans, A.G., 1980, Elastic/plastic indentation damage in ceramics: the median/radial crack system, *J. Am. Ceram. Soc.*, Vol. 63, pp. 574–581.
13. Chiang, S.S., Marshall, D.B., and Evans, A.G., 1982, The response of solids to elastic/plastic indentation. I. Stresses and residual stresses, *J. Appl. Phys.*, Vol. 53(1), pp. 298–311.
14. Chiang, S.S., Marshall, D.B., and Evans, A.G., 1982, The response of solids to elastic/plastic indentation. II. Fracture initiation, *J. Appl. Phys.*, Vol. 53(1), pp. 312–317.
15. Marshall, D.B., Lawn, B.R., and Evans, A.G., 1982, Elastic/plastic indentation damage in ceramics: the lateral crack system, *J. Am. Ceram. Soc.*, Vol. 65, pp. 561–566.
16. Marshall, D.B., 1983, Controlled flaws in ceramics: a comparison of Knoop and Vickers indentation, *J. Am. Ceram. Soc.*, Vol. 66, pp. 127–131.
17. Marshall, D.B., 1984, Geometric effects in elastic/plastic indentation, *J. Am. Ceram. Soc.*, Vol. 67, pp. 57–60.
18. Samuels, L.E. and Mulhearn, T.O., 1957, An experimental investigation of the deformed zone associated with indentation hardness impressions, *J. Mech. Phys. Solids*, Vol. 5, p. 125.
19. Van Der Zwaag, S., Hagan, J.T., and Field, J.E., 1980, Studies of contact damage in polycrystalline zinc sulphide, *J. Mater. Sci.*, Vol. 15, pp. 2965–2972.

20. Marshall, D.B., 1983, Surface damage in ceramics: implications for strength degradation, erosion and wear, *Nitrogen Ceramics*, Riley, F.L., Ed., Nijhoff, The Hague, p. 635.
21. Marshall, D.B., Evans, A.G., Yakub Khuri, B.T., Tien, J.W., and Kimo, G.S., 1983, The nature of machining damage in brittle materials, *Proc. Roy. Soc. London*, Vol. A835, p. 461.
22. Lawn, B.R., Hockey, B.J., and Ritcher, H., 1983, Indentation analysis: applications in the strength in wear of brittle materials, *J. Microscopy*., Vol. 130, Pt. 3, p. 259.
23. Samuel, R. and Chandrasekar, S., 1989, Effect of residual stresses on the fracture of ground ceramics, *J. Am. Ceram. Soc*., Vol. 72, pp. 1960–1966.
24. Ahn, Y., Chandrasekar, S., and Farris, T.N., 1993, Measurement of residual stresses in machined ceramic using the indentation technique, *NIST SP* 847, pp. 135–146.
25. Hakulinen, M., 1985, Residual strength of ground hot isostatically pressed silicon nitride, *J. Mater. Sci*., Vol. 20, pp. 1049–1060.
26. Petrovic, J.J., Dirks, R.A., Jacobson, L.A., and Mendiratta, M.G., 1976, Effects of residual stresses on fracture from controlled surface flaws, *J. Am. Ceram. Soc*., Vol. 59, pp. 177–178.
27. Swain, M.V., 1976, A note on the residual stress about a pointed indentation impression in a brittle solid, *J. Mater. Sci*., Vol. 11, pp. 2345–2347.
28. Ota, M. and Miyahara, K., 1990, The influence of grinding on the flexural strength of ceramics, *4th Int. Grinding Conf*., SME Technical Paper MR90–537.
29. Conway, J.C., Jr. and Kirchner, H.P., 1980, The mechanics of crack initiation and propagation beneath a moving sharp indentor, *J. Mater. Sci*., Vol. 15, pp. 2879–2883.
30. Cheng, W., Ling, E., and Finnie, I., 1990, Median cracking of brittle solids due to scribing with sharp indentors, *J. Am. Ceram. Soc*., Vol. 73, pp. 580–586.
31. Kirchner, H.P., 1984, Comparison of single-point and multipoint grinding damage in glass, *J. Am. Ceram. Soc*., Vol. 67, pp. 347–353.
32. Kirchner, H.P., 1984, Damage penetration at elongated machining grooves in hot pressed Si_3N_4, *J. Am. Ceram. Soc*., Vol. 67, pp. 127–132.
33. Mayer, J.E., Jr. and Fang, G.P., 1993, Diamond grinding of silicon nitride, *NIST SP* 847, pp. 205–222.
34. Mecholsky, J.J., Freiman, S.W., and Rice, R.W., 1977, Effect of surface finish on strength of fracture of glass, *11th Int. Congress on Glass*, Prague, Czechoslovakia.
35. Thomas, M.B., West, R.D., and West, W.E., 1987, A study of selected grinding parameters on the surface finish and strength of hot pressed silicon nitride, *Intersociety Symp. on Machining of Adv. Ceramic Mater. and Components*, American Ceramic Society, pp. 218–234.
36. Miyasato, H., Okamoto, H., Usui, S., Miyamoto, A., and Ueno, Y., 1989, The effect of grinding on strength of hot-pressed silicon nitride, *ISIJ Int*., Vol. 29(9), pp. 726–733.
37. Andersson, C.A. and Bratton, R.J., 1979, Effect of surface finish on the strength of hot pressed silicon nitride, in *The Science of Ceramic Machining and Surface Finishing* II, *NBS Special Publication* 562, pp. 463–476.
38. Unno, K. and Imai, T., 1987, Performance of diamond wheel in grinding ceramics, *Proc. 6th Int. Conf. on Prod. Eng*., Osaka, pp. 26–32.
39. Kawamura, H., 1991, Study of grinding process and strength for ceramic heat insulated engine, *Superabrasives 91*, SME, pp. 9–1 to 9–7.
40. Spur, G. and Tio, T.H., 1988, Surface layer damage in grinding of advanced engineering ceramics, *Trans. NAMRC/SME* XVI, pp. 224–231.

41. Matsuo, Y., Ogasawara, T., and Kimura, S., 1987, Statistical analysis of the effect of surface grinding on the strength of alumina using Weibull's multi-modal function, *J. Mater. Sci.*, Vol. 22, pp. 1482–1488.
42. Hawman, M.W., Cohen, P.H., Conway, J.C., and Paangborn, R.N., 1985, The effect of grinding on the flexural strength of a sialon ceramic, *J. Mater. Sci.*, Vol. 20, pp. 482–490.
43. Kachanov, M. and Montagut, E., 1986, Interaction of a crack with certain micro-crack arrays, *Eng. Frac. Mech.*, Vol. 25, pp. 625–636.
44. Hu, K.X. and Chandra, A., 1993, A fracture mechanics approach to modeling strength degradation in ceramic grinding processes, *ASME J. Eng. Ind.*, Vol. 115, pp. 73–84.
45. Evans, A.G. and Marshall, D.B., 1981, Wear mechanisms in ceramics, *Fundamentals of Friction and Wear of Materials*, Rigney, D.A., Ed., ASME, pp. 439–452.
46. Koepke, B.G. and Strokes, R.J., 1979, Effect of workpiece properties on grinding forces in polycrystalline ceramics, in *The Science of Ceramic Machining and Surface Finishing* II, *NBS Special publication* 562, p. 75.
47. Kirchner, H.P. and Conway, J.C., 1985, Mechanisms of material removal and damage penetration during single point grinding of ceramics, *Machining of Ceramic Materials and Components*, ASME, New York, Vol. 17, pp. 53–61.
48. Larchuk T.J. Conway, J.C., Jr., and Kirchner, H.P., 1985, Crushing as a mechanism of material removal during abrasive machining, *J. Am. Ceram. Soc.*, Vol. 68, pp. 209–215.
49. Conway, J.C., Jr. and Kirchner, H.P., 1986, Crack branching as a mechanism of crushing during grinding, *J. Am. Ceram. Soc.*, Vol. 69, pp. 603–607.
50. Imanaka, A., Fujino, S., and Maneta, S., 1972, Direct observation of material removal process during grinding of ceramics by micro-flash technique, in *The Science of Ceramic Machining and Surface finishing*, *NBS Special Publication* 348, p. 37.
51. Huerta, M. and Malkin, S., 1976, Grinding of glass: the mechanics of the process, *ASME J. Eng. Ind.*, pp. 459–467.
52. Huerta, M. and Malkin, S., 1976, Grinding of glass: surface structure and fracture strength, *ASME J. Eng. Ind.*, pp. 468–473.
53. Pai, D.M., Ratterman, E., and Shaw, M.C., 1989, Grinding swarf, *Wear*, Vol. 131, pp. 329–339.
54. Zhang, B. and Howes, T.D., 1994, Material-removal mechanisms in grinding ceramics, *Ann. CIRP*, Vol. 43/1, pp. 305–308.
55. Zhang, B. and Howes, T.D., 1995, Subsurface evaluation of ground ceramics, *Ann. CIRP*, Vol. 44/1, pp. 263–266.
56. Toh, S.B. and McPherson, R., 1986, Fine scale abrasive wear of ceramics by a plastic cutting process, in *Science of Hard Materials, Inst. Phys. Conf.* Serf. No. 75, Chap. 9, Adam Higler, Ltd., Rhode, pp. 865–871.
57. Yoshikawa, M., Bi, Z., and Tokura, H., 1987, Observations of ceramic surface cracks by newly proposed methods, *J. Ceram. Soc., Jpn. Int. Ed.*, Vol. 95, pp. 911–918.
58. Zhang, B., Tokura, H., and Yoshikawa, M., 1988, Study on surface cracking of alumina scratched by single-point diamonds, *J. Mater. Sci.*, Vol. 23, pp. 3214–3224.
59. Johansson, S. and Schweitz, J., 1988, Contact damage in single-crystalline silicon investigated by cross-sectional transmission electron microscopy, *J. Am. Ceram. Soc.*, Vol. 71, pp. 617–623.

60. Tönshoff, H.K., Telle, R., and Roth, P., 1990, Chip formation and material removal in grinding of ceramics, *4th Int. Grinding Conf.*, SME Technical Paper MR90–539.
61. Brinksmeier, E., Preub, W., and Riemer, O., 1995, From friction to chip removal: an experimental investigation of micro cutting process. Part II: Ductile to brittle transition in monocrystalline silicon and germanium, *Proc. 8th Int. Prec. Eng. Sem.*, pp. 335–338, Compiegne, France.
62. Nakajima, T., Uno, Y., and Fujiwara, Y., 1989, Cutting mechanism of fine ceramics with a single point diamond, *Prec. Eng.*, Vol. 11, pp. 19–25.
63. Matsuo, T., Toyoura, S., Oshima, E., and Ohbuchi, Y., 1989, Effect of grain shape on cutting forces in superabrasive single-grit tests, *Ann. CIRP*, Vol. 38/1, pp. 323–326.
64. Xu, H.H.K., Jahanmir, S., and Wang, Y., 1995, Effect of grain size on scratch interactions and material removal in alumina, *J. Am. Ceram. Soc.*, Vol. 78, pp. 881–891.
65. Hwang, T.W. and Malkin S., 1999, Grinding mechanisms and energy balance for ceramics, *ASME J. Manuf. Sci. Eng.*, Vol. 121, pp. 623–631.
66. Singhal, S.C., 1976, Effect of water vapor on the oxidation of hot pressed silicon nitride and silicon carbide, *J. Am. Ceram. Soc.*, Vol. 59, pp. 81–82.
67. Zarudi, I. and Zhang, L.C., 1997, Subsurface structure change of silicon after ultra-precision grinding, *Advances in Abrasive Technology*, Zhang, L.C. and Yasunaga, N., Eds., World Scientific, Singapore, pp. 33–37.
68. Malkin, S., 1989, *Grinding Technology: Theory and Application of Machining with Abrasives*, John Wiley & Sons, New York. Reprinted by SME.
69. Spur, G., Stark, C., and Tio, T.H., 1985, Grinding of non-oxide ceramics using diamond grinding wheels, *Machining of Ceramic Materials and Components*, Subramanian, K. and Komanduri, R., Eds., PED-Vol. 17, ASME, p. 33.
70. Subramanian, K. and Keat, P.P., 1985, Parametric study on grindability of structural and electronic ceramics. Part I: *Machining of Ceramic Materials and Components*, Subramanian, K. and Komanduri, R., Eds., PED-Vol. 17, ASME, p. 25.
71. Inasaki, I. and Nakayama, K., 1986, High-efficiency grinding of advanced ceramics, *Ann. CIRP*, Vol. 35/1, pp. 211–214.
72. Chen, C., Jung Y., and Inasaki, I., 1989, Surface, cylindrical and internal grinding of advanced ceramics, *Grinding Fundamentals and Applications*, Malkin, S. and Kovach, J.A., Eds., PED-Vol. 39, ASME, pp. 201–211.
73. Kitajima, K., Kai, G.Q., Kumagai, N., Tanaka, Y., and Zheng, H.W., 1992, Study on mechanism of ceramics grinding, *Ann. CIRP*, Vol. 41/1, pp. 367–371.
74. Roth, P. and Tönshoff, H.K., 1993, Influence of microstructure on grindability of alumina ceramics, *NIST SP* 847, pp. 247–261.
75. Zhang, L.C., 1994, Grindability of some metallic and ceramic materials in CFG regimes, *Int. J. Mach. Tools Manufact.*, Vol. 34, No. 8, pp. 1045–1057.
76. Bifano, T.G., Dow, T.A., and Scattergood, R.O., 1991, Ductile regime grinding: a new technology for machining brittle materials, *ASME J. Eng. Ind.*, Vol. 113, pp. 184–189.
77. Hwang, T.W., 1997, Grinding energy and mechanisms for ceramics, PhD Thesis, University of Massachusetts.

4

Grinding of Ceramics with Attention to Strength and Depth of Grinding Damage

J.E. Mayer Jr.

CONTENTS

ABSTRACT Experimental grinding research has led to information regarding ground strength of the ceramic and depth of damage in the ceramic caused by grinding. Diamond wheel grit size and machine parameters of wheel depth of cut, workspeed, and wheelspeed in surface grinding were investigated. The investigated ceramic materials are hot-pressed silicon nitride, reaction-bonded silicon nitride, aluminum oxide, and silicon carbide. Results provide methodology to achieve maximum ground strength and to use damage depth information to minimize grinding time.

4.1 Introduction

Advanced engineering structural ceramics are in demand for various applications, especially for the automotive industry due to their outstanding high-temperature capacity, wear resistance, chemical resistance, and lower weight-to-strength ratio than metals. The high-temperature capacity of a ceramic engine allows fuel to be burned at higher temperature, which gives a better fuel efficiency. The better strength-to-weight ratio of ceramic material can reduce the weight of the engine and further enhance the fuel efficiency by reducing the overall weight of the vehicle. The excellent wear resistance of advanced engineering ceramic materials makes them the best candidates for applications such as industrial seals and bearings. Table 4.1 lists some applications of advanced structural ceramic materials. Recently, a diesel engine manufacturer reported the production of ceramic fuel injection pins, and an auxiliary turbine manufacturer is producing ceramic seals for its gas turbine engines.

Some of the most common advanced structural ceramics include aluminum oxide (alumina), silicon nitride, silicon carbide (SiC), and zirconium oxide (zirconia). Table 4.2 shows the sales distribution of major advanced ceramic items [1]. This table indicates that structural ceramics account for one-third of the $20 billion market, and this market is growing. Since advanced structural ceramics are the hardest among all the materials and some of them such as aluminum oxide and SiC are the most broadly used materials for making abrasives and conventional grinding wheels for grinding metals, it is therefore very difficult to machine these materials. By far, the grinding process with diamond grinding wheels is the only effective way of final shaping the advanced structural ceramics [2]. As a result of this, the machining cost can be from 70% to 90% of the total component cost [3]. In addition, the brittleness of the ceramic material makes it extremely vulnerable to incur microcracks during the grinding process, which can result in a highly inhomogeneous distribution in structural strength of the machined component [4].

TABLE 4.1

Applications of Advanced Structural Ceramic Materials

Applications of Advanced Structural Ceramics					
Textile machine parts	Bearings	Catalyst supports	Filters	Nozzles	Rolling jigs
Laboratory equipment	Burners	Cutting tools	Heaters	Port liners	Thermal insulators
Wear resistant parts	Casting dies	Drawing dies	Medical implants	Protection tubes Fuel injection pins	
Turbo charger wheels	Coil forms	Extrusion dies	Membranes	Pump parts	Seals
	Potential Applications				
	Engine Components		**Gas Turbine Parts**		
Bearings	Glow plugs	Diesel particulate traps	Bearings	Heat exchanger	Shrouds
Cylinder liners	Manifolds	Piston caps and rings	Blades	Housing	Stators
Prechamber	Tappets	Valves and seats	Heat shields	Rotor and shaft	

It is well known that the material removal mechanism in the grinding of ceramics is mainly a brittle fracturing process and grinding induced damage in terms of microcracks has been observed in various ceramics. Ceramic materials are very sensitive to cracks due to their low fracture toughness. The principal induced crack systems are the lateral cracks and the median cracks. The lateral cracks are parallel to the ground surface, and the median

TABLE 4.2

World Wide Advanced Ceramic Industry Sales

Major Items (Percentage Numbers in Parentheses are Based on 1994 Data)	**1993 (in Billions)**	**1994 (in Billions)**
Engineering structural ceramics (32%) Electrical and electronic ceramics (21%) Capacitors, substrates, and packages (20%) Electrical porcelain (5%) Bioceramics (1%) Others (21%)	$18.3 Total	$20.2 Total

cracks are perpendicular to the surface. The lateral cracks have been used to explain the material removal process and the median cracks to explain strength degradation [5,6].

This paper describes experimental grinding research, which has led to information regarding the ground strength of the ceramic and the depth of damage in the ceramic caused by grinding. Results provide methodology to achieve maximum ground strength and to use damage depth information to minimize grinding time.

4.2 Ceramic Materials

The ceramic materials investigated in this paper are hot-pressed silicon nitride (HPSN), reaction-bonded silicon nitride (RBSN), zirconia-toughened alumina (Al_2O_3), and porous SiC. The available material properties for these ceramics are given in Table 4.3. The HPSN and zirconia-toughened alumina ceramics were in the shape of flexural strength test bars cut from billets. The RBSN ceramic was molded into bars of the shape of flexural test specimens. The porous SiC ceramic was provided in the shape of flexural test specimens.

4.3 Experimental Procedure

4.3.1 Grinding

Surface grinding was employed to determine the ground strength of the ceramics and the depth of damage caused by the grinding process. Two

TABLE 4.3

Ceramic Material Properties

	HPSN	RBSN	Zirconia-Toughened Al_2O_3	Porous SiC
Grain size (μm)	—	1–2	1	—
Density (g/cm^3)	3.2	2.36	4.38	—
Porosity	<1%	20%	<0.5%	19.5%
Elastic modulus, E (GPa)	310	200	340	—
Vickers Hardness, H (GPa)	17.9	6.8	16.5	—
Flexural strength (MPa)	800	205	925	145
Fracture Toughness, K_{IC} (MPa m$^{\frac{1}{2}}$)	4.7	2.5	4.5	—
Brittleness, H/K_{IC} (m$^{-\frac{1}{2}}$)	3808	2720	3667	—

commercial surface grinders were used, one with microprocessor control on the wheel depth of cut which could be controlled at a unit of 1.27 microns. The other had computer numerical control (CNC) on all axes where the wheel depth of cut could be controlled at a unit of 0.254 microns. A water miscible synthetic grinding fluid was used with a concentration ratio of 1:30.

Resinoid-bonded diamond grinding wheels with 152.4 mm outer diameter and with different grit sizes were employed. The grit surface density was measured in this work by means of an optical microscope sighting on the grit flats after wheel truing and dressing. The grinding wheels were trued with a commercial diamond roll truing device and were dressed with aluminum oxide dressing sticks. Truing and dressing procedures were standardized and were as those recommended by the diamond grinding wheel supplier. For the truing process, each wheel is mounted on its own hub, which is not removed during the life of the wheel. The wheel is adjusted in the hub to make it concentric with the grinder spindle using a dial indicator, the outer surface of the wheel is coated with a permanent ink marker, and the wheel is trued until all the ink markings have been removed. By this truing process, the grinding wheel is expected to run quite precisely. The effect of wheel runout on the depth of cut that each grit takes has been estimated at about 2%–4%, or less, for the test conditions employed.

4.3.2 Grit Depth of Cut

The value of grit depth of cut, h_{max}, depends on both machine and wheel parameters. Equation 4.1 was used to compute the value of h_{max} in this research. This expression for h_{max} was proposed by Shaw, Reichenbach, and Mayer [7,8,9]. Figure 4.1 illustrates

$$h_{max} = \sqrt{\frac{4v_w}{v_c C r}} \sqrt{\frac{a_e}{d_s}}, \tag{4.1}$$

where h_{max} is the grit depth of cut (maximum undeformed chip thickness), C is the number of active cutting points per unit area of the wheel periphery (grit surface density), r is the ratio of chip width to average undeformed chip thickness, v_c is the wheel peripheral speed, v_w is the workpiece speed (table speed), a_e is the wheel depth of cut, and d_s is the wheel diameter.

The value of r is reported to be in the range of 10–20 [7]; but in this paper, r was assumed to be 10.

4.3.3 Strength Testing

Flexural strength tests were performed in accordance with MIL-STD-1942 (MR) [10,11] on all bars that are ground in this research. For HPSN ceramic,

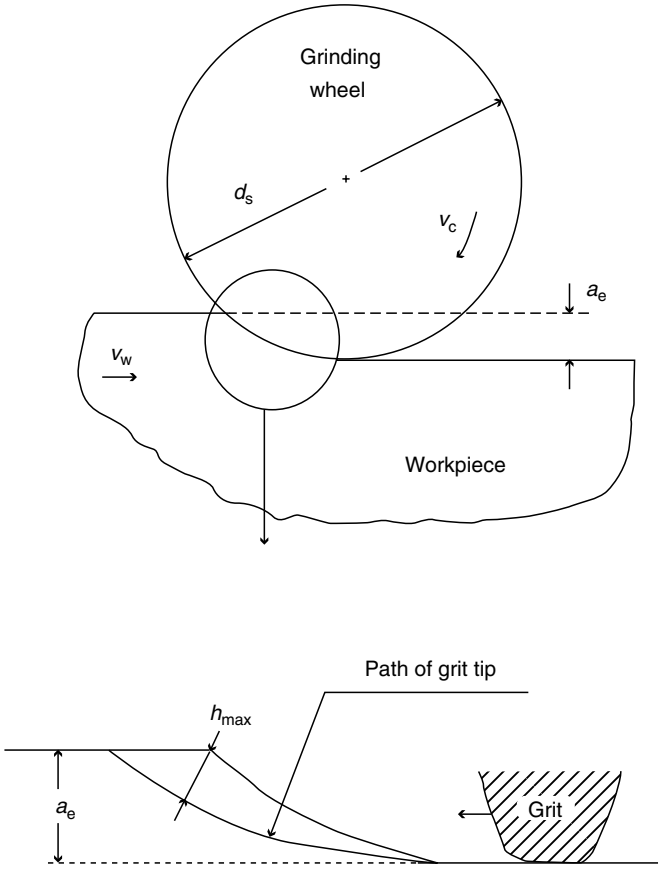

FIGURE 4.1
Illustration of the surface grinding process showing various process variables.

a total of five bars were tested for each grinding condition to establish the flexural strength. For the other ceramic materials, 10 bars were tested for each grinding condition to establish the flexural strength. The Weibull characteristic strength was used to present the results in this investigation.

4.3.4 Lapping

Ceramic workpieces, which have been ground under conditions that degrade the strength, can be brought back up to maximum strength by removing the damaged surface layer. The damaged layer can be removed by the lapping process, which is a low-stress process and imposes no further damage as it removes layers of surface. Diamond lapping was employed in this research to establish the depth of damage as a function of grinding grit depth of cut.

A lapping system equipped with a 15 in. copper lap plate and an electronically controlled diamond slurry dispenser was used in this research. A 3 μm diamond slurry was employed, which produced higher and more stable material removal rate than a 1 μm diamond slurry. The slurry was applied at a rate of 3 sec of spray every 30 sec. The lapping pressure on each ceramic test bar was 35,700 Pa. A sample carrier accommodated five test bars arranged around the outer perimeter of the carrier.

Only one lapping station (ring) was employed at a time because that gave better control over a consistent lapping process than using all three stations. Using these lapping conditions, a consistent depth removal rate of 0.01 mm in 20 min was achieved lapping the alumina ceramic. The copper lap plate needed reconditioning after every 20 min of use to reproduce a rough surface texture to entrap and embed diamond grits to perform the cutting action. A 140- or 170-mesh diamond-conditioning ring was employed, which gave higher material removal rate than a 120- or 140-mesh diamond-conditioning ring. The reconditioning time employed was 1–2 min.

4.3.5 Grinding Procedure for Determining Ground Strength

For investigating ground strength of HPSN and RBSN ceramics, the grit sizes of the wheels employed are shown in Table 4.4. The wheels have a concentration of 150 and an uncoated diamond. The width and thickness of the diamond layer are 3.17 mm.

For grinding of HPSN ceramic, the test conditions employed for finish grinding are shown in Table 4.5. The machine parameter of width of grind was held constant at $b_b = 1.59$ mm, and the wheel speed, v_c, was held constant at 24.7 m/sec. For test condition numbers 1, 2, 6, 7, and 8, five bars were ground with the grind direction longitudinal to the length of the bar, and another set of five bars were ground transverse to the bar length. For the other test conditions, the grind direction was either longitudinal or transverse (see Table 4.5).

For the grinding of RBSN ceramic, the test conditions employed for finish grinding are shown in Table 4.6. The machine parameter of width of grind was held constant at $b_b = 1.59$ mm. For test condition number 2 through

TABLE 4.4

Grit Size of Diamond Grinding Wheels

Wheel	Grit Mesh Size	Mean Grit Size (μm)	Grit Surface Density (#/mm^2)
D4/8MIC-R150	1200	5.1	49.91
SDG320-R150	320	50.8	27.59
SDG180-R150	180	87.5	11.66
SDG110-R150	110	152	8.324
SDG100-R150	100	249	6.402

TABLE 4.5

Test Conditions for HPSN Ceramic

Test Condition	HPSN Batch	Wheel Grit Size d_k (μm)	Table Feed v_w (mm/sec)	Depth of Cut a_e (mm)	Grind Direction	Grit Depth of Cut h_{max} (μm)
1	A	5.1	7.62	0.0013	L and T	0.0845
2	A	50.8	7.62	0.0025	L and T	0.1351
3	B	50.8	7.62	0.0025	L	0.1351
4	B	152	1.02	0.0254	T	0.1600
5	B	152	4.56	0.0013	T	0.1600
6	A	87.5	7.62	0.0025	L and T	0.2079
7	A	152	7.62	0.0025	L and T	0.2460
8	A	249	7.62	0.0025	L and T	0.2850
9	B	152	4.56	0.0254	T	0.3380
10	B	152	25.4	0.0508	T	0.95
11	B	152	80.43	0.0051	T	0.95
12	B	152	127.0	0.1270	T	2.67

Note: L represents longitudinal and T represents transverse.

number 8, ten bars were ground with the grind direction longitudinal to the length of the bar, and another set of ten bars were ground transverse to the bar length. For test condition number 1, the grinding direction was transverse. A similar procedure was employed to determine the ground strength of zirconia-toughened Al_2O_3 and porous SiC ceramics.

4.3.6 Grinding Procedure for Determining Damage Depth

For determining the depth of damage caused by the grinding of RBSN and zirconia-toughened alumina, the ceramic materials were first ground under a range of grit depth of cut conditions and then lapped to establish the depth

TABLE 4.6

Test Conditions for RBSN Ceramic

Test Condition	Wheel Grit Size d_k (μm)	Wheel Speed v_c (m/sec)	Table Feed v_w (mm/sec)	Depth of Cut a_e (mm)	Grit Depth of Cut h_{max} (μm)
1	50.8	47.1	2.00	0.0025	0.0500
2	50.8	39.9	6.73	0.0025	0.1000
3	50.8	24.7	7.62	0.0025	0.1351
4	87.5	24.7	7.62	0.0025	0.2079
5	152	24.7	7.62	0.0025	0.2460
6	249	24.7	7.62	0.0025	0.2805
7	152	31.9	36.4	0.0508	1.000
8	152	31.9	119.4	0.0762	2.000

TABLE 4.7

Grit Sizes of Diamond Grinding Wheels

Wheel	Grit Mesh Size	Mean Grit Size (μm)	Grit Surface Density (#/mm^2)
SD320-R100	320	50.8	29.07
SD110-R100	110	152	6.13

of grinding damage. Resinoid-bonded diamond wheels with a concentration of 100 were employed for the grinding phase. Table 4.7 shows the two different diamond grit sizes used. The wheel diameter was 152.4 mm.

The grinding conditions used for finish grinding in this research are shown in Table 4.8 and Table 4.9. Table 4.8 is for the grinding conditions for RBSN ceramic and Table 4.9 is for the alumina ceramic. The grind directions were perpendicular to the direction of the tensile stress in the subsequent flexural strength test, which is ground transverse to the length of the bar.

The procedure employed for determining the depth of damage caused by grinding is as follows. Large samples of 40 or more test workpieces are ground at each grinding test condition. The test workpieces ground at a given test condition are then subdivided into groups of five. The first group of five is flexural strength tested as ground. The Weibull characteristic strength is computed and is used as the strength of that group. The second group is lapped to a depth removed of either 0.0127 mm or 0.0254 mm as a starting point and strength tested. The depth removed by lapping is measured with a digital micrometer. The subsequent groups are lapped to incrementally increasing depths of material removal and then strength tested. A plot of flexural strength versus depth of material removed by lapping is made, and the lapped depth at which maximum strength is reached is taken as the effective damage depth for that particular grinding test condition. This lapping and strength testing procedure is then repeated for each test condition. This lapping and strength testing approach for experimentally determining the depth of damage induced in ceramics by the grinding process was previously employed by Spur [4] and Inasaki [12].

TABLE 4.8

Grinding Test Conditions for RBSN Ceramic

Test Condition No.	Wheel Grit Size d_k (μm)	Wheel Speed v_c (m/sec)	Table Feed v_w (mm/sec)	Depth of Cut a_e (mm)	Grit Depth of Cut h_{max} (μm)
1	50.8	47.1	2.12	0.0025	0.05
2	50.8	39.9	7.62	0.0025	0.10
3	152	24.7	7.62	0.0025	0.29
4	152	24.7	30.1	0.0508	1.20
5	152	24.7	119.4	0.0762	2.66

TABLE 4.9

Grinding Test Conditions for Zirconia Toughened Alumina Ceramic

Test Condition No.	Wheel Grit Size d_k (μm)	Wheel Speed v_c (m/sec)	Table Feed v_w (mm/sec)	Depth of Cut a_e (mm)	Grit Depth of Cut h_{max} (μm)
1	152	47.9	7.5	0.0025	0.23
2	152	39.9	14	0.0025	0.35
3	152	39.9	30	0.0051	0.61
4	152	31.9	80	0.0127	1.4
5	152	27.9	140	0.0381	2.6

4.4 Results and Discussion

4.4.1 Ground Strength

4.4.1.1 HPSN Ceramic

The flexural strength test results for HPSN ceramic for all the test conditions (test condition number 1 through number 12) are shown plotted against h_{max} in Figure 4.2 and Figure 4.3. Two curves are shown, one for longitudinal grinding and the other for transverse grinding. For longitudinal grinding, the flexural tensile stress was applied parallel to the grinding direction. For transverse grinding, the flexural stress was applied perpendicular to the grinding direction. The data point symbols, which are circles (either open or

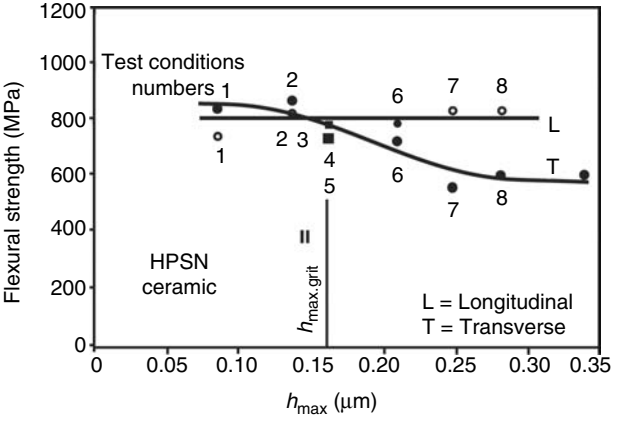

FIGURE 4.2

Flexural strength as a function of grit depth of cut, h_{max} (test condition number 1 through number 9), for HPSN ceramic.

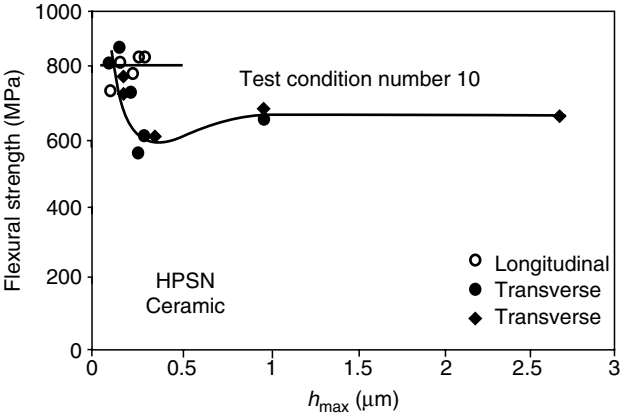

FIGURE 4.3
Flexural strength as a function of grit depth of cut, h_{max} (test condition number 1 through number 12), for HPSN ceramic.

solid circles), are for test conditions where only the wheel grit size was varied. The other data point symbols are for test conditions where only the machine parameters of workpiece speed and wheel depth of cut were varied. The data shown in Figure 4.2 were previously published by Mayer and Fang [13].

From Figure 4.2 and Figure 4.3, it can be seen that for grinding in the longitudinal direction there is little or no loss of strength as h_{max} increases for the range that is investigated. However, for transverse grinding, there is a decrease in strength as h_{max} increases beyond a critical value of h_{max} of about 0.160 μm. Figure 4.2 identifies this critical value of h_{max}.

It is concluded from Figure 4.2 and Figure 4.3 that the controlling factors regarding flexural strength are grind direction and wheel grit depth of cut, h_{max}. Additionally, a critical h_{max} value exists for maximum ground strength, and for HPSN this critical h_{max} value is about 0.160 μm.

4.4.1.2 RBSN Ceramic

Flexural strength test results for RBSN ceramic for test condition numbers. 1–8 are shown plotted against h_{max} in Figure 4.4 and Figure 4.5. Two curves are shown in these figures, one for longitudinal grinding and the other for transverse grinding. The data point symbols, which are circles (either open or solid), are for test conditions where only the wheel grit size was varied (test condition numbers 3 through number 6). The other data point symbols are for test conditions where only the machine parameters were varied.

Since h_{max} is solely a geometric factor, there might be concerns that thermal effects could also be a controlling factor. It should be observed that test condition number 1 is operating at near the maximum safe wheel speed for the resinoid-bonded grinding wheel employed in this research.

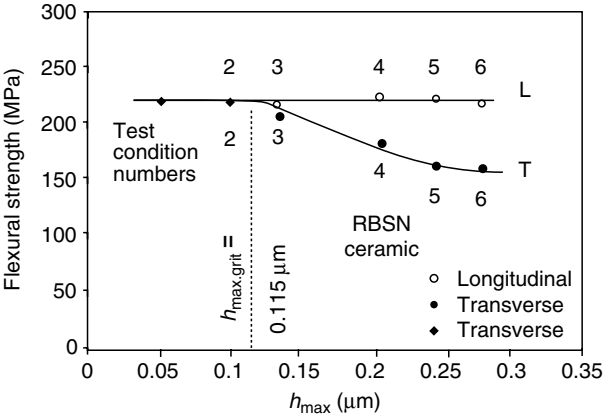

FIGURE 4.4
Flexural strength as a function of grit depth of cut, h_{max} (test condition number 1 through number 6), for RBSN ceramic.

From Figure 4.4 and Figure 4.5, it can be seen that for grinding in the longitudinal direction there is little or no loss of strength as h_{max} increases for the range that is investigated. For transverse grinding, there is a decrease in strength as h_{max} increases beyond a critical value of h_{max} of about 0.115 μm. Figure 4.4 identifies this critical value of h_{max}. The data in Figure 4.4 and Figure 4.5 were previously reported by Mayer and Fang [14].

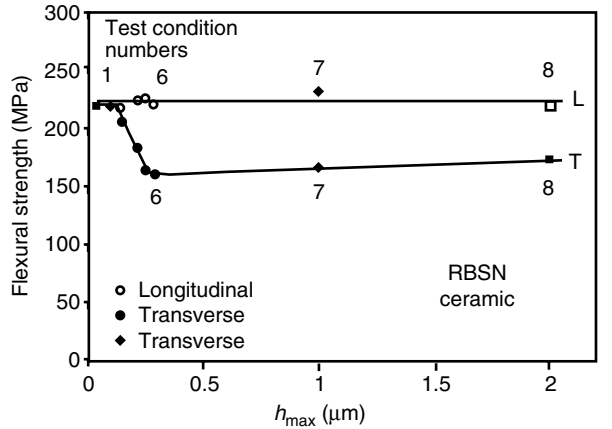

FIGURE 4.5
Flexural strength as a function of grit depth of cut, h_{max} (test condition number 1 through number 8), for RBSN ceramic.

Test condition numbers 2, 7, and 8 are also operating at elevated wheel speeds. Since the flexural strength data points for test condition numbers 1, 2, 7, and 8 fall along the same curves as for the lower wheel speed conditions (test condition number 1 through number 6), it appears that a thermal effect is not related to flexural strength for normal grinding conditions with ceramics.

It is concluded from Figure 4.4 and Figure 4.5 that the controlling factors regarding flexural strength are grind direction and wheel grit depth of cut, h_{max}, for the range of test conditions employed. Additionally, a critical h_{max} value exists for maximum ground strength, and for RBSN this critical h_{max} value is about 0.115 μm.

By comparing Figure 4.2 through Figure 4.5, it is seen that both ceramic materials have similar trends regarding flexural strength versus h_{max}. The higher inherent strength of HPSN is reflected in the higher maximum flexural strength for HPSN than that of RBSN. Note that each of these ceramic materials has its own value for critical grit depth of cut.

4.4.1.3 Other Ceramics

Grinding investigations have been conducted on other ceramics, namely zirconia-toughened alumina and porous SiC (19.5% porous), which further confirm the importance of the grit depth of cut, h_{max}, in regard to flexural strength of the ground ceramic. Figure 4.6 and Figure 4.7 show flexural strength versus h_{max} results for zirconia-toughened alumina. Although additional research is necessary, it is quite apparent that the critical h_{max} value is 0.05–0.1 μm or less for this ceramic. Note the substantial reduction in flexural strength as the critical h_{max} value is exceeded. Zirconia-toughened

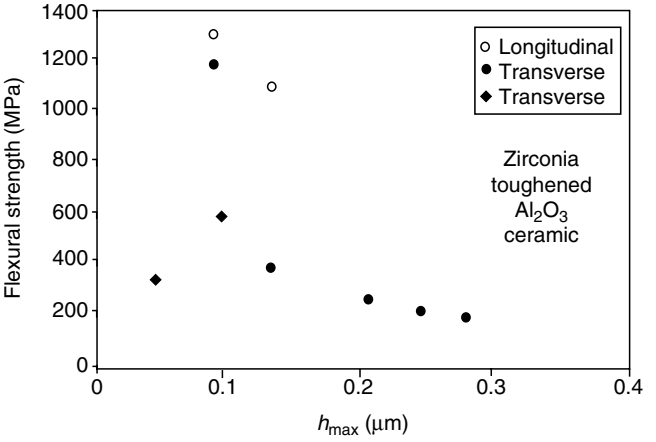

FIGURE 4.6
Flexural strength as a function of grit depth of cut, h_{max} (h_{max} up to 0.28 μm), for zirconia-toughened Al_2O_3 ceramic.

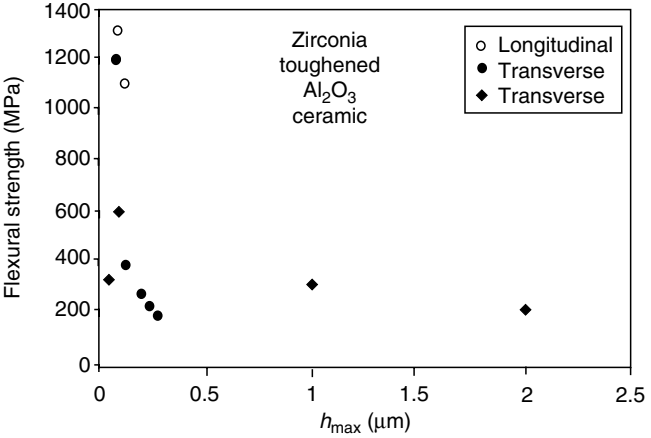

FIGURE 4.7
Flexural strength as a function of grit depth of cut, h_{max} (h_{max} up to 2.0 μm), for zirconia-toughened Al_2O_3 ceramic.

alumina can have high flexural strength; however, to achieve this it must be ground at an h_{max} value equal to or less than the critical value.

Results for the porous SiC are shown in Figure 4.8. It is seen from this figure that the flexural strength has not dropped off even at rather high h_{max} values. Figure 4.8 indicates that the critical h_{max} value for this ceramic is greater than 3.5 μm. This porous SiC has low, but very consistent strength regardless of the h_{max} value within normal grinding conditions.

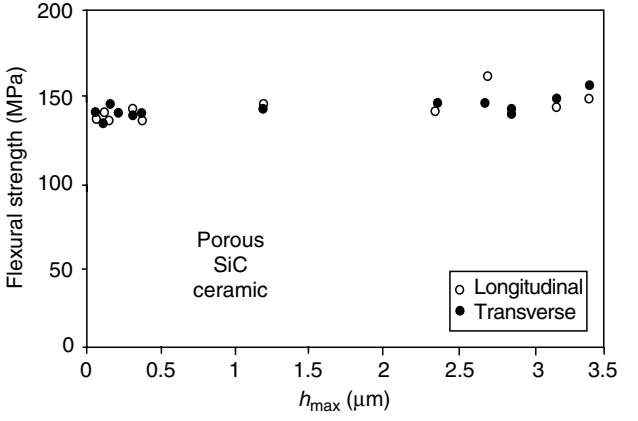

FIGURE 4.8
Flexural strength as a function of grit depth of cut, h_{max}, for porous SiC ceramic.

4.4.1.4 Guidelines for Efficient High-Strength Finish Grinding

Guidelines for efficient high-strength finish grinding of ceramics were previously published by Mayer and Fang [15]. The guidelines are developed using the data in Figure 4.2 through Figure 4.8, Equation 4.1, and the concept that it is best to employ the highest value of h_{max} to achieve higher grinding removal rates. This concept for maximum strength grinding means that

$$h_{max} = h_{max.grit}, \tag{4.2}$$

where $h_{max.grit}$ is the largest h_{max} value for which maximum strength occurs.

4.4.1.5 Physical Meaning of Critical Grit Depth of Cut

The physical interpretation of flexural strength versus h_{max} curves in Figure 4.2 through Figure 4.8 is that when h_{max} becomes small enough to cause the cracks induced by the grinding process to diminish in size equal to or smaller than those inherent in the ceramic material; then no reduction in strength will occur. In that case, maximum strength will occur.

As the size of the induced cracks is related to the stress imposed by each grinding grit, which is in turn related to the grit depth of cut, it is expected that the critical grit depth of cut should be controlled by fracture mechanics principles. Key material properties in fracture mechanics analysis as reported by Kirchner and Larchuk [16], Ota and Miyahara [17], and Veldkamp et al. [18] are fracture toughness (K_{IC}), hardness (H), and elastic modulus (E). Note also the large difference in porosity in these materials, which must also play a role. Only by a comprehensive fracture mechanics analysis can an analytical model for critical h_{max} regarding flexural strength be developed.

4.4.2 Depth of Damage

4.4.2.1 RBSN Ceramic

Figure 4.9a through Figure 4.9e show plots of flexural strength versus depth of material removed by lapping for RBSN ceramic for the grinding test conditions of h_{max} of 0.05, 0.10, 0.29, 1.20, and 2.66 μm, respectively. Note that when the grinding damage is removed, the strength reaches a rather consistent maximum value with further lapping depth removed. From Figure 4.9a through Figure 4.9e the effective grinding damage depth can be read. Figure 4.4 and Figure 4.5 show that the maximum strength for RBSN ceramic is 220 MPa. Figure 4.9a through Figure 4.9b are at maximum strength and therefore lapping is not expected to change the strength, and thus for h_{max} of 0.05 and 0.10 μm, the effective grinding damage depth is taken as 0 μm. Figure 4.9c through Figure 4.9e increase asymptotically to maximum strength.

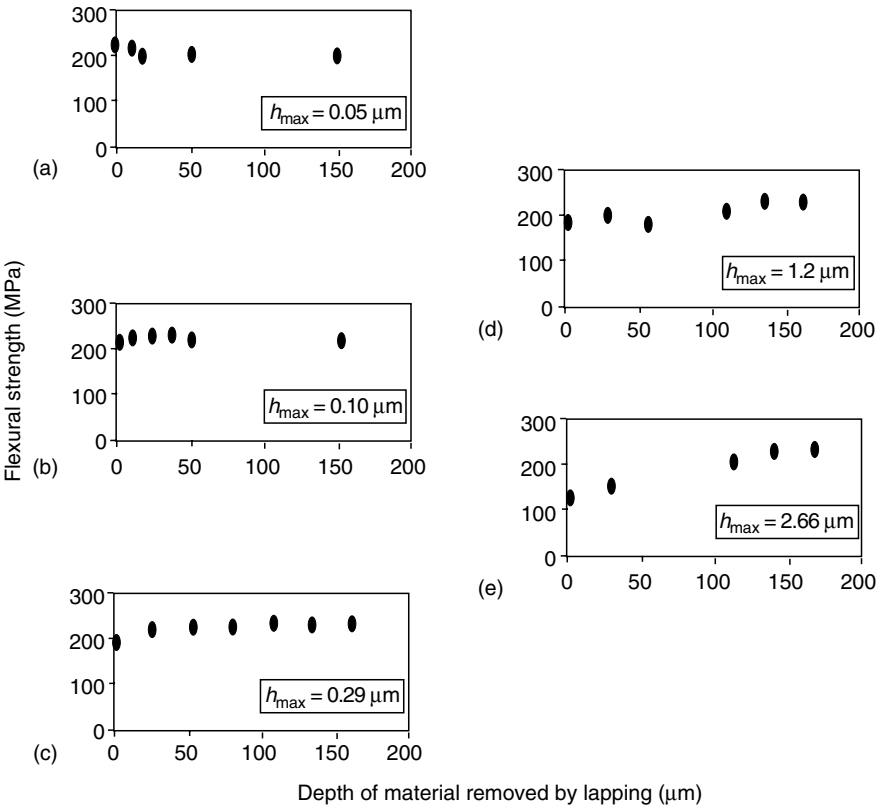

FIGURE 4.9
Flexural strength vs. depth of material removed by lapping for RBSN ceramic with original surface ground at (a) $h_{max} = 0.05$ μm, (b) $h_{max} = 0.10$ μm, (c) $h_{max} = 0.29$ μm, (d) $h_{max} = 1.20$ μm, and (e) $h_{max} = 2.26$ μm.

The grinding depth of damage is shown plotted against the grinding test conditions, h_{max}, in Figure 4.10 for RBSN ceramic as determined from Figure 4.9a through Figure 4.9e. The depth of damage shown in Figure 4.10, determined by the lapping method, is an effective depth of damage because it is based on flexural strength rather than on a direct measurement of the damage depth. From Figure 4.10, the effective grinding damage depth for RBSN ceramic appears to be 100–125 μm. The authors do not have a good explanation for the constant depth of damage at the larger grit depths of cut; perhaps residual stresses might be a factor.

4.4.2.2 Zirconia-Toughened Alumina Ceramic

Flexural strength versus depth of material removed by lapping results for zirconia-toughened alumina ceramic are shown in Figure 4.11a through

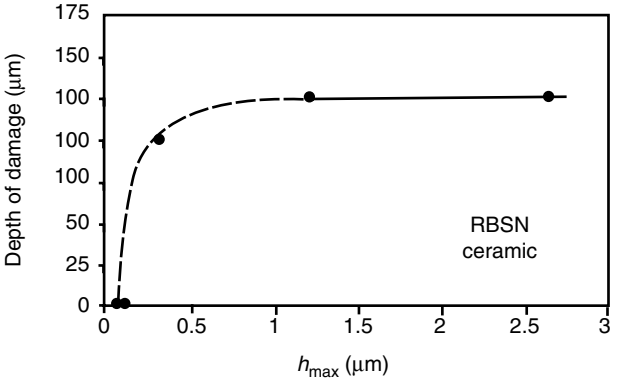

FIGURE 4.10
Depth of damage determined by the lapping method for RBSN ceramic.

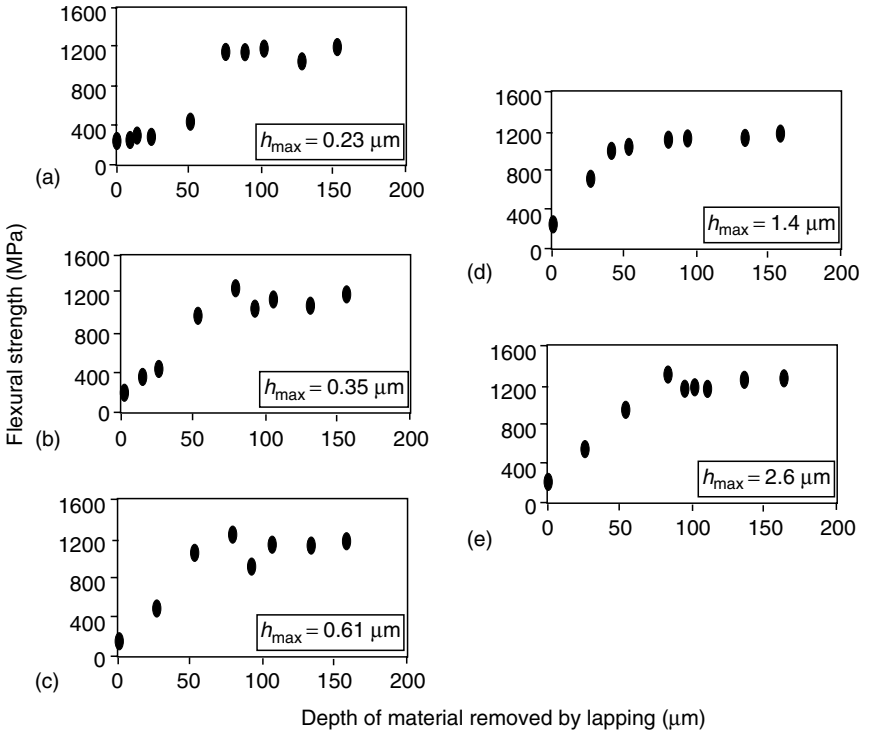

FIGURE 4.11
Flexural strength vs. depth of material removed by lapping for RBSN ceramic with original surface ground at (a) $h_{max} = 0.23$ μm, (b) $h_{max} = 0.35$ μm, (c) $h_{max} = 0.61$ μm, (d) $h_{max} = 1.4$ μm, and (e) $h_{max} = 2.6$ μm.

Figure 4.11e for the grinding test conditions of h_{max} of 0.23, 0.35, 0.61, 1.4, and 2.6 μm, respectively. Again, when the grinding damage is removed, the strength reaches a rather consistent maximum value with further lapping depth removed. From Figure 4.11a through Figure 4.11e the effective grinding damage depth was read.

The grinding depth of damage versus the grinding test conditions, h_{max}, results are shown in Figure 4.12 for zirconia-toughened alumina ceramic as determined from Figure 4.11a through Figure 4.11e. The effective depth of damage at h_{max} of about 0.1 μm, i.e., the critical h_{max} where maximum strength is reached during grinding is assumed to be 0 μm. From Figure 4.12, the effective grinding damage depth for zirconia-toughened alumina ceramic appears to be 75 μm.

The depth of damage was also computed based on the measured as-ground flexural strength and fracture mechanics [19]. The computed values for depth of damage are 165, 291, 271, 127, and 201 μm, respectively for the h_{max} values of 0.23, 0.35, 0.61, 1.4, and 2.6 μm. Although the computed values are of the right order of magnitude, it is concluded that the computed depth of damage is not as reliable as the depth of damage determined by the lap and strength test method.

Zhang and Howes [20] made direct measurements of the depth of grinding damage by an inspection process using SEM combined with an etching technique. They investigated other ceramics, namely, HPSN, hot-pressed alumina, and sintered SiC. Their results indicate that the damage depth increases exponentially with increases in grit depth of cut, h_{max}. They reported that the depth of damage for h_{max} of about 1 μm is 16 μm for SiC, 32 μm for alumina, and 42 μm for silicon nitride. The Zhang and Howes results are not based on strength data, whereas the results in this paper are effective depths of damage based on flexural strength.

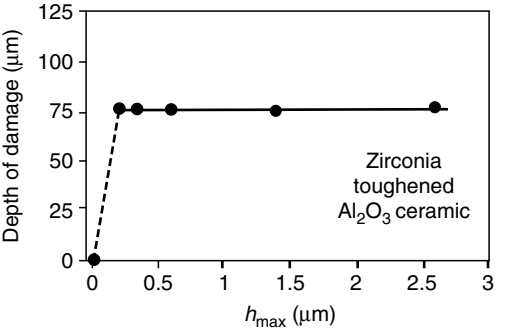

FIGURE 4.12
Depth of damage determined by the lapping method for zirconia-toughened alumina ceramic.

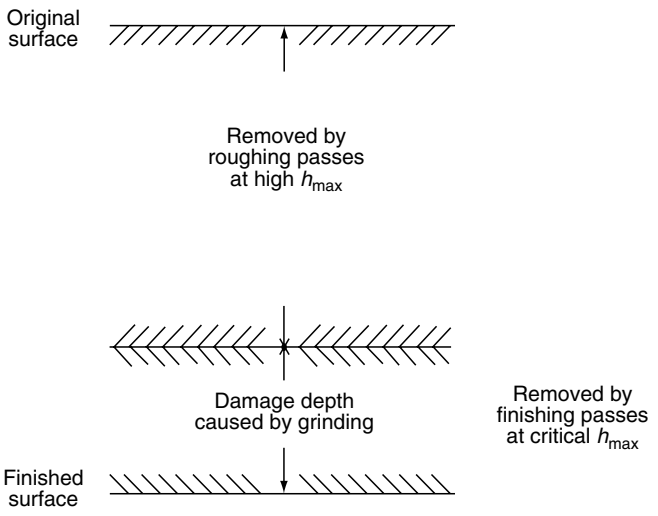

FIGURE 4.13
Strategy for minimum grinding time.

4.4.2.3 Strategy for Minimum Grinding Time

The plots of depth of damage versus h_{max} in Figure 4.10 and Figure 4.12 suggest a strategy for high removal rate grinding while achieving maximum strength. This strategy is rough grind at high h_{max} leaving an amount of finish stock equal to the damage imposed by the rough grinding, then finish grind at the critical h_{max} to remove the roughing damage and to achieve maximum strength. Figure 4.13 illustrates this strategy. By rough grinding at the highest h_{max} available on the grinding equipment, maximum removal rate is achieved for roughing. By finish grinding at the critical h_{max} value, maximum removal rate for finish grinding is achieved. Therefore, the shortest (or minimum) grinding time for completing both the roughing and finishing operations is achieved. To apply this strategy, the depth of damage needs to be established by means of an experimental method such as the lapping approach. Fortunately, the depth of damage appears to be a constant with increasing h_{max} values.

4.5 Conclusions

From the results of this research, the following conclusions regarding the grinding of ceramics can be drawn:

1. The controlling factors influencing flexural strength of ground ceramics appear to be grind direction and wheel grit depth of cut, h_{max}.

2. For longitudinal grinding, i.e., when the grinding direction is parallel to the applied tensile stress, the wheel grit depth of cut, h_{max}, has no effect on the flexural strength.
3. For transverse grinding, i.e., when the grinding direction is perpendicular to the applied tensile stress, the flexural strength drops off when the wheel grit depth of cut, h_{max}, is increased beyond a critical value.
4. Each ceramic material appears to have its own critical h_{max} value.
5. The lapping and strength testing approach can be used to experimentally determine the effective depth of damage caused by grinding of ceramics.
6. With the knowledge of the depth of damage, a strategy is proposed for high removal rate grinding including both roughing and finishing while still achieving maximum strength.

References

1. Ceramic Industry 1994, 1995.
2. McEachron, R.W. and Lorence, S.C., Superabrasives and structural ceramics in creep-feed grinding, *Ceramic Bulletin*, Vol. 67, No. 6, 1988, pp. 1031–1036.
3. Spur, G., Creep Feed Grinding of Advanced Engineering Ceramics, Note FER 08c, Production Technology Center Berlin, Pascalstrabe 8–9, D-1000 Berlin 10, 1990.
4. Konig, W., Cronjager, L., Spur, G., Tonshoff, H.-K., Vigneau, M., and Zdeblick, W.J., Machining of New Materials, *Annals of the CIRP*, Vol. 39/2, 1990, pp. 673–681.
5. Lawn, B.R. and Marshall, D.B., Indentation fracture and strength degradation in ceramics, *Fracture Mechanics of Ceramics, Vol. 3: Flaws and Testing*, Bradt, R.C., Hasselman, D.P.H. and Lange, F.F., Eds., Plenum Press, 1978.
6. Malkin, S. and Ritter, J.E., Grinding mechanisms and strength degradation for ceramics, *Intersociety Symposium on Machining of Advanced Ceramic Materials and Components*, ASME, 1988, pp. 57–72.
7. Kalpakjian, S., *Manufacturing Engineering and Technology*, Addision-Wesley Publishing Co., Reading, MA, 1989.
8. Reichenbach, G.S., Mayer, J.E., Kalpakcioglu, S., and Shaw, M.C., The role of chip thickness in grinding, *Trans. ASME*, Vol. 18, 1956, pp. 847–850.
9. Tonshoff, H.K., Peters, J., Inasaki, I., and Paul, T., Modelling and simulation of grinding processes, *Annals of the CIRP*, Vol. 41/2, 1992, pp. 677–688.
10. MIL-STD-1942(MR), Flexural Strength of High Performance Ceramics at Ambient Temperature, Department of the Army, Washington, DC, 1983.
11. Quinn, G.D., Baratta, F.I., and Conway, J.A., Commentary on U.S. Army Standard Test Method for Flexural Strength of High Performance Ceramics at Ambient Temperature, AD-A160 873, AMMRC 85-21, Army Material and Mechanics Research Center, Watertown, MA 02172-0001, 1985.